



HAL
open science

Numerical investigations on the role of the $\mu(I)$ viscoplastic rheology and the 3D frictional effects on a granular column collapse on large slopes

Nathan Martin, Ioan Ionescu, Anne Mangeney, Maxime Farin

► To cite this version:

Nathan Martin, Ioan Ionescu, Anne Mangeney, Maxime Farin. Numerical investigations on the role of the $\mu(I)$ viscoplastic rheology and the 3D frictional effects on a granular column collapse on large slopes. 2015. hal-01204716v1

HAL Id: hal-01204716

<https://hal.science/hal-01204716v1>

Preprint submitted on 24 Sep 2015 (v1), last revised 19 Nov 2016 (v4)

HAL is a multi-disciplinary open access archive for the deposit and dissemination of scientific research documents, whether they are published or not. The documents may come from teaching and research institutions in France or abroad, or from public or private research centers.

L'archive ouverte pluridisciplinaire **HAL**, est destinée au dépôt et à la diffusion de documents scientifiques de niveau recherche, publiés ou non, émanant des établissements d'enseignement et de recherche français ou étrangers, des laboratoires publics ou privés.

Numerical investigations on the role of the $\mu(I)$ viscoplastic rheology and the 3D frictional effects on a granular column collapse on large slopes

N. Martin,¹ I. R. Ionescu,^{2,3} A. Mangeney,^{1,4} and M. Farin¹

¹*Institut de Physique du Globe de Paris, Seismology Team, University Paris-Diderot, Sorbonne Paris Cité, France*

²*LSPM, University Paris-Nord, Sorbonne-Paris-Cité, France*

³*IMAR, Romanian Academy, Bucharest, Romania*

⁴*ANGE Team, CEREMA, INRIA, Lab. J. Louis Lions, Paris, France*

(Dated: July 28, 2015)

The present work focuses on the modeling of dry granular flows in the context of the granular column collapse in an inclined channel and detailed comparison with experimental thickness profiles and front velocities. A nonlinear Coulomb friction term, representing the friction on the lateral walls of the channel is added in the model, providing the ability to accurately simulate this column collapse on large slopes (up to 22°). We demonstrate that accounting for lateral friction effect in the simulations is crucial at large slopes (higher or equal to 16°).

In other respect, we show that a Drucker-Prager constant viscosity model with a well-chosen value for the viscosity is able to predict the slow propagation phase at large slopes, experimentally observed, whereas the viscosity provided by the $\mu(I)$ rheology, evaluated from physical quantities, does not behave as well.

Finally, we show that the present model predicts the appearance of shear bands in the bulk when refining the mesh. This behaviour appears to be unstable (as it induces shear bands as narrow as 4 grain diameter, to the best of our refining capacities) but is not affecting the simulations in terms of velocity range and free-surface movements. We also show that this effect is triggered by the coupling of the plasticity criterion with the pressure field.

I. INTRODUCTION

Granular materials play a major role in many branches of natural and industrial physics. Dry granular flows can exhibit solid, liquid or gas state, hysteretic behaviour, wall effects, depending on the flowing context. The description of the mechanical behaviour of this media still remains a challenging question and the ability to achieve accurate numerical simulations of the flow of a granular material strongly depends on the discrimination and description of the physical quantities involved in these flows.

In the context of geophysical flows such as landslides and debris flows, most of the numerical work has been performed using thin-layer depth-averaged approximations to overcome the prohibitive computational burden of solving the 3D primitive equations problem. In general, these works have proved to be efficient in simulating the final deposit of the flow. However, the dynamical evolution of the granular mass along the flow is not adequately described by shallow approximations. In addition, mechanical processes such as the static-flowing transition are not accurately handled by thin-layer depth averaged model. We refer to Bingham³, GRD Midi Group³², Andreotti et al.², Ancey¹ for general reviews on granular flows.

The mechanical investigation of these flows, based on a complete 3D modelling, at a laboratory scale, is a relevant way to study and quantify the processes at

stake in such a flow and validate or improve the constitutive relations that are being used. In this context, the experimental and numerical study of the granular column collapse has become widely used for the study of the dynamics and deposit of gravity granular flows. The reason is that it has a typical and reproducible transient behavior. It starts with a quick acceleration phase, that lasts until a maximum velocity is reached. After what, the flow begins to decelerate during a longer period, until it stops. The different phases of the flow, the shape of the final deposit and the runout distance are the main features that numerical models try to reproduce. Their duration and shape change with the slope of the bottom, the aspect ratio of the initial column, the possible presence of an erodible bed, etc.

As a matter of fact, many numerical studies addressed granular column released problem using typically three different approaches: shallow-type models (Mangeney-Castelnau et al.²⁶, Kerswell²¹, Larieu et al.²⁵, Doyle et al.⁸), Discrete Element Methods (DEM) (Staron and Hinch³⁷, Zenit³⁹, Lacaze et al.²³, Girolami et al.¹¹), and complete viscous-plastic models (Crosta et al.⁵, Lacaze and Kerswell²², Meruane et al.³¹ and Lagrée et al.²⁴).

While thin-layer depth averaged models are generally able to lead to a good agreement with experiments for the final deposit shape, they strongly overestimate the flow velocity during the acceleration phase (see *e.g.* Mangeney-Castelnau et al.²⁶, Kerswell²¹, Ionescu¹⁷). Discrete Element method have been more able to

quantitatively reproduce the column spreading with well-chosen friction coefficient values (see Lariou et al.²⁵, Lacaze and Kerswell²², Girolami et al.¹¹) but often overestimate the runout distance (see Staron and Hinch³⁷, Lagr e et al.²⁴). In addition, all these studies focus on the collapse on an horizontal plane, and mostly on the reproduction of scaling laws, with little attention paid to the dynamic.

A first attempt to thoroughly compare the dynamics of the simulations with a continuum viscoplastic approach to experimental results (typically by comparing thickness profiles during the collapse) is proposed by Ionescu et al.¹⁸. They successfully achieve an accurate prediction of the whole spreading of the column on an horizontal plane using values of the literature for the physical parameters. However, difficulties arose for the simulation of the collapse on an inclined plane ($\alpha = 16^\circ$) with an overestimated runout distance.

The present work is based on the same numerical model and focuses on the simulation of the granular column collapse on large slopes. The comparisons with experiments are based on the experimental setup and the resulting data of Mangeney et al.²⁷ and Farin et al.⁹. The model presented in Ionescu et al.¹⁸ has been improved only by considering additional physics without any adjustment on the physical parameters of the model. In a first part, we briefly describe the model and the approach considered to include lateral friction effects in a $2D$ model. In a second part, simulations are compared with experiments in terms of thickness profiles and front velocities, showing that the new model allows to achieve systematic quantitative simulations of the column collapse on various slopes (up to 22°) demonstrating the important role of the friction on the lateral walls, in order for the granular mass to stop.

Also, following Ionescu et al.¹⁸, the preliminary results on the little effects of the variable viscosity provided by the $\mu(I)$ rheology model compared to a constant viscosity Drucker-Prager viscoplastic model are carried on in the present work. In a third part, thickness profiles, front velocities are compared for both model on different slopes, demonstrating that the average value of the viscosity term can be of great influence on the dynamic of the flow, whereas its spatial variability is not. An analytical pressure profile derived from a constant viscosity Drucker-Prager model is used to try to highlight the differences of this model with the $\mu(I)$ rheology with variable viscosity.

On a fourth part, we present preliminary results on the development of shear bands in the computational domain when one refines the mesh. This phenomenon appears to be unstable (as it is not captured when refining the mesh). We show that it is triggered by the coupling of the plasticity criterion with the solution of

the problem through the pressure dependency. However, as showed, these instabilities do not affect the result in terms of velocity range and thickness profile of the domain but modify the internal structure of the velocity field and the pressure field.

Finally, we discuss the results and give some conclusions on their implications in terms of rheological modelling and numerical simulations.

The first appendix provides a short description of the numerical scheme employed in all the computations. The second appendix develops the change of referential of an analytical pressure field from the topography related frame to the horizontal-vertical one.

II. MECHANICAL MODEL

A granular material generally exhibits a plastic behavior that prevents the medium from deforming if the applied stress is lower than a given value called yield stress. This effect is modelled using a plasticity criterion that describes this flow/no-flow behavior. In the specific case of a granular material, the plasticity criterion is a frictional criterion in the sense that its ability to sustain a Cauchy stress $\boldsymbol{\sigma}$ is due to internal friction between grains and geometrical particle rearrangement.

A classical approach consists in using the Drucker-prager plasticity criterion κ that relates the pressure field p to the deviatoric stress tensor $\boldsymbol{S} = p\mathbf{Id} + \boldsymbol{\sigma}$ through :

$$\|\boldsymbol{S}\| = \kappa(p) = \kappa_0 + \mu p, \quad (1)$$

where $\|\boldsymbol{A}\| = \sqrt{\boldsymbol{A} : \boldsymbol{A}/2}$ is the Frobenius matrix norm, or equivalently the second invariant of the tensor \boldsymbol{A} , $\mu = \tan(\delta)$ is the tangent of the internal friction angle and κ_0 is the cohesion of the material (set to 0 here).

The deformation of the material occurring under a large enough stress is given by a plastic flow law that makes the hypothesis of the colinearity of the deviatoric stress tensor \boldsymbol{S} and the strain-rate tensor $\boldsymbol{D} = \frac{1}{2}(\nabla\mathbf{u} + \nabla\mathbf{u}^T)$ where $\mathbf{u} = (u_x, u_y)$ denotes the 2D velocity field. This property is written :

$$\frac{\boldsymbol{S}}{\|\boldsymbol{S}\|} = \frac{\boldsymbol{D}}{\|\boldsymbol{D}\|}, \quad (2)$$

that becomes using the Drucker-Prager plasticity criterion (1) :

$$\boldsymbol{S} = \mu p \frac{\boldsymbol{D}}{\|\boldsymbol{D}\|}. \quad (3)$$

By analogy to a viscous flow law, the term $\mu p/\|\boldsymbol{D}\|$ can be seen as an effective viscosity of the material

depending on shear rate and pressure.

This purely plastic behavior is known to fail describing correctly the flow of granular materials. To overcome this problem, one uses the so-called $\mu(I)$ rheology that phenomenologically describes a spatial variability of the internal friction coefficient μ from various physical quantities and one dimensionless quantity called the inertial number I . The inertial number, which is the square root of the Savage number or of the Coulomb number, introduced by Savage³⁵ and Ancey et al.¹ respectively, is defined by :

$$I = \frac{2\|\mathbf{D}\|d}{\sqrt{p/\rho_s}}, \quad (4)$$

where d denotes the grain diameter and ρ_s the grain density. This number can be seen as the ratio between two timescales : the microscopic timescale of particle rearrangement $d/\sqrt{p/\rho_s}$ and the macroscopic strain rate time scale $1/\|\mathbf{D}\|$.

The $\mu(I)$ rheology is then written :

$$\mu(I) = \mu_1 + \frac{\mu_2 - \mu_1}{1 + \frac{I_0}{I}} \quad (5)$$

where I_0 is a dimensionless constant and μ_1 and μ_2 represent respectively the value of the internal friction coefficient for low and high inertial numbers. This law has been introduced by Jop et al.¹⁹.

As in Ionescu et al.¹⁸, we develop the plastic flow law (3) with $\mu = \mu(I)$ defined by (5) and (4), and we finally obtain (setting $k = d\sqrt{\rho_s}$):

$$\mathbf{S} = \mu_1 p \frac{\mathbf{D}}{\|\mathbf{D}\|} + 2 \frac{(\mu_2 - \mu_1)p}{2\|\mathbf{D}\| + I_0\sqrt{p}/k} \mathbf{D} \quad (6)$$

In that form the flow law is now including the original pressure-dependent plastic term $\mu_1 p \mathbf{D}/\|\mathbf{D}\|$ plus an additional viscous term $2\eta \mathbf{D}$ introducing a spatially varying viscosity η given by:

$$\eta = \frac{(\mu_2 - \mu_1)p}{2\|\mathbf{D}\| + I_0\sqrt{p}/k} \quad (7)$$

Consequently, the use of the $\mu(I)$ law to describe the internal friction coefficient in the plastic flow law leads to describe the granular material as a viscoplastic fluid with a pressure-dependent yield stress and spatially variable viscosity depending on the pressure and the shear-rate.

In what follows, the role of the spatial variation of η defined by (7) is being assessed and compared to the case of a constant viscosity η . To avoid confusion, the $\mu(I)$ rheology will designate the original definition

given by (5) and the variable viscosity η , defined by (7), obtained by developing the $\mu(I)$ rheology will be referred to as η_I (although η , as defined by (7), does not directly depends on the inertial number I but on the physical parameters that are involved in the calculation of I).

To sum-up, the rewriting of the $\mu(I)$ rheology naturally leads to the following variable viscosity Drucker-Prager formulation:

$$\mathbf{S} = \mu(I)p \frac{\mathbf{D}}{\|\mathbf{D}\|} = \kappa(p) \frac{\mathbf{D}}{\|\mathbf{D}\|} + 2\eta_I \mathbf{D} \quad (8)$$

This law is eventually inverted in order to express the strain-rate \mathbf{D} as a function of the deviatoric stress \mathbf{S} leading to:

$$\mathbf{D} = \frac{1}{2\eta_I} \left[1 - \frac{\kappa(p)}{\|\mathbf{S}\|} \right]_+ \mathbf{S}, \quad (9)$$

The above expressions was introduced by Perzyna³³ and Duvaut and Lions⁷ and is called the viscoplastic regularization method. We refer to Section A for the description of the numerical treatment of the viscoplastic flow law (9).

III. MASS AND MOMENTUM CONSERVATION

The granular column collapse is a highly transient problem with an aspect ratio close to 1 at the beginning of the collapse. For these reasons, it is modelled here by a complete Navier-Stokes problem with free-surface transport. The viscoplastic fluid is considered to be incompressible. The solution (\mathbf{u}, p) of the Navier-Stokes equation is computed in a domain $\Omega(t)$ by solving the following system :

$$\begin{cases} \rho(\partial_t \mathbf{u} + (\mathbf{u} \cdot \nabla) \mathbf{u}) - \text{div}(\mathbf{S}) + \nabla p = \rho \mathbf{g}, \\ \text{div}(\mathbf{u}) = 0. \end{cases} \quad (10)$$

The viscoplastic fluid domain $\Omega(t)$ is transported with the fluid as:

$$\frac{\partial 1_{\Omega(t)}}{\partial t} + \mathbf{u} \cdot \nabla 1_{\Omega(t)} = 0 \quad (11)$$

where $1_{\Omega(t)}$ is the characteristic function of the domain.

IV. BOUNDARY CONDITIONS

The bidimensionnal fluid domain $\Omega(t)$ represents the central vertical cross-section of the granular flow in the channel (see Figure 1). Its boundary $\partial\Omega(t)$ is divided into two disjoint parts $\partial\Omega(t) = \Gamma_b \cup \Gamma_s$. On the boundary

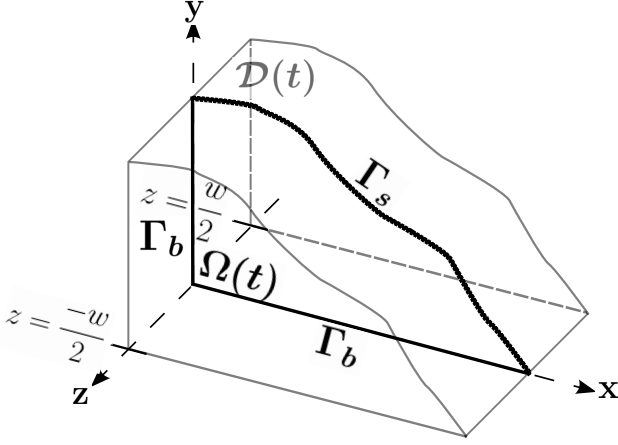


Figure 1. Fluid domain and notations

Γ_b , the flowing material is in contact with a rigid body through the Coulomb friction law :

$$\mathbf{u} \cdot \mathbf{n} = 0, \begin{cases} \boldsymbol{\sigma}_T = -\mu [-\boldsymbol{\sigma}_n]_+ \frac{\mathbf{u}_T}{|\mathbf{u}_T|} & \text{if } \mathbf{u}_T \neq 0 \\ |\boldsymbol{\sigma}_T| \leq \mu [-\boldsymbol{\sigma}_n]_+ & \text{if } \mathbf{u}_T = 0 \end{cases} \quad (12)$$

where μ is the Coulomb friction coefficient at the boundary, \mathbf{n} is the outward normal vector on $\partial\Omega(t)$, and $[\]_+$ is the positive part. We adopt the following notation for the normal and tangential components of the velocity \mathbf{u} and the normal stress $\boldsymbol{\sigma}\mathbf{n}$:

$$\mathbf{u} = u_n \mathbf{n} + \mathbf{u}_T \text{ and } \boldsymbol{\sigma}\mathbf{n} = \sigma_n \mathbf{n} + \boldsymbol{\sigma}_T \quad (13)$$

A stress-free condition is imposed at the surface Γ_s :

$$\boldsymbol{\sigma}\mathbf{n} = 0. \quad (14)$$

V. ACCOUNTING FOR LATERAL FRICTION

To include the three dimensional effect of friction on the lateral walls of the channel, let us consider the 3D domain $\mathcal{D}(t) = \Omega(t) \times [-\frac{w}{2}, \frac{w}{2}]$ where w denotes the channel width. The solution is assumed to be constant in the transverse direction z (see Figure 1). The weak formulation of the problem is then evaluated on $\mathcal{D}(t)$ and the variational formulation is modified accordingly.

Let the variational formulation of problem (10) with boundary conditions (12) and (14) on $\mathcal{D}(t)$ be:

$$\rho \int_{-\frac{w}{2}}^{\frac{w}{2}} \int_{\Omega(t)} (\partial_t \mathbf{u} + \mathbf{u} \cdot \nabla \mathbf{u}) \cdot \boldsymbol{\varphi} \, dx + \int_{-\frac{w}{2}}^{\frac{w}{2}} \int_{\Omega(t)} \nabla p \cdot \boldsymbol{\varphi} \, dx = \int_{-\frac{w}{2}}^{\frac{w}{2}} \int_{\Omega(t)} \operatorname{div}(\mathbf{S}) \cdot \boldsymbol{\varphi} \, dx + \rho \int_{-\frac{w}{2}}^{\frac{w}{2}} \int_{\Omega(t)} \rho \mathbf{g} \cdot \boldsymbol{\varphi} \, dx \quad \forall \boldsymbol{\varphi} \in H. \quad (15)$$

where H designates the appropriate functional space and $\boldsymbol{\varphi}$ a test function of this space.

It becomes using Green's formula:

$$\begin{aligned} \rho w \int_{\Omega(t)} (\partial_t \mathbf{u} + \mathbf{u} \cdot \nabla \mathbf{u}) \cdot \boldsymbol{\varphi} \, dx + w \int_{\Omega(t)} \nabla p \cdot \boldsymbol{\varphi} \, dx = \\ -w \int_{\Omega(t)} \mathbf{S} : \mathbf{D}(\boldsymbol{\varphi}) \, dx + \rho w \int_{\Omega(t)} \rho \mathbf{g} \cdot \boldsymbol{\varphi} \, dx \\ + \int_{\partial\mathcal{D}(t)} \boldsymbol{\sigma}\mathbf{n} \cdot \boldsymbol{\varphi} \, dx \quad \forall \boldsymbol{\varphi} \in H. \end{aligned} \quad (16)$$

The boundary term coming from Green's formula is written:

$$\int_{\partial\mathcal{D}(t)} \boldsymbol{\sigma}\mathbf{n} \cdot \boldsymbol{\varphi} \, dx = w \int_{\Gamma_b} \boldsymbol{\sigma}\mathbf{n} \cdot \boldsymbol{\varphi} \, ds + 2 \int_{\Omega(t)} \boldsymbol{\sigma}\mathbf{n} \cdot \boldsymbol{\varphi} \, dx. \quad (17)$$

We retrieve the 1D boundary integral of the 2D variational formulation multiplied by the width of the channel w plus an extra volumic term. In this mixed 2D/3D form, the tangential component of the normal stress $\boldsymbol{\sigma}_T$ is defined by:

$$\boldsymbol{\sigma}_T = \begin{cases} \sigma_{t_1} \mathbf{t}_1 + \sigma_{t_2} \mathbf{t}_2 & \text{in 3D,} \\ \sigma_t \mathbf{t} & \text{in 2D.} \end{cases} \quad (18)$$

On the lateral faces, the normal component σ_n of the normal stress $\boldsymbol{\sigma}\mathbf{n}$ is naturally equal to the third diagonal component of the stress tensor σ_{zz} . Using both 2D incompressibility ($\partial_x u_x + \partial_y u_y = 0$) and 3D incompressibility ($\partial_x u_x + \partial_y u_y + \partial_z u_z = 0$), we easily obtain that $\partial_z u_z = 0$ and consequently:

$$\sigma_{zz} = -p. \quad (19)$$

From (12) and (19), the boundary term (17) becomes:

$$\begin{aligned} \int_{\partial\mathcal{D}(t)} \boldsymbol{\sigma}\mathbf{n} \cdot \boldsymbol{\varphi} \, dx = w \int_{\Gamma_b} \boldsymbol{\sigma}\mathbf{n} \cdot \boldsymbol{\varphi} \, ds \\ + 2 \left(\int_{\Omega(t)} -pz \cdot \boldsymbol{\varphi} \, dx - \int_{\Omega(t)} \mu p \frac{\mathbf{u}}{|\mathbf{u}|} \, dx \right) \end{aligned} \quad (20)$$

The solution being constant in the direction z , $\int_{\Omega(t)} -pz \cdot \boldsymbol{\varphi} \, dx = 0$. If we divide the variational formulation by the width w , we finally obtain:

$$\begin{aligned} \rho \int_{\Omega(t)} (\partial_t \mathbf{u} + \mathbf{u} \cdot \nabla \mathbf{u}) \cdot \boldsymbol{\varphi} \, dx + \int_{\Omega(t)} \nabla p \cdot \boldsymbol{\varphi} \, dx = \\ - \int_{\Omega(t)} \mathbf{S} : \mathbf{D}(\boldsymbol{\varphi}) \, dx + \rho \int_{\Omega(t)} \rho \mathbf{g} \cdot \boldsymbol{\varphi} \, dx \\ + \frac{2}{w} \int_{\Omega(t)} \mu p \frac{\mathbf{u} \cdot \boldsymbol{\varphi}}{|\mathbf{u}|} \, dx - \int_{\Gamma_b} \mu [\boldsymbol{\sigma}_n]_+ \frac{\mathbf{u}_T}{|\mathbf{u}_T|} \cdot \boldsymbol{\varphi} \, ds \quad \forall \boldsymbol{\varphi} \in H. \end{aligned} \quad (21)$$

It corresponds to the original 2D variational formulation plus the volumic frictional term

$$\frac{1}{w} \mu p \frac{2\mathbf{u}}{|\mathbf{u}|}. \quad (22)$$

It is worth noticing that a simpler approach to take into account the effect of lateral friction that consists in increasing the value of the internal friction coefficient leads to a somewhat similar correction. This approach consists in modelling the effect of the sidewalls by introducing an additional friction coefficient with a maximum value of the order of $\mu \frac{h}{w}$ where h is the thickness of the flowing layer, μ is the grain/wall friction coefficient and w is the width of the channel (see equation (1) of Taberlet et al.³⁸ or equation (4.5) of Jop et al.²⁰). Indeed, if one replaces μ_1 and μ_2 by respectively $(\mu_1 + \mu \frac{h}{w})$ and $(\mu_2 + \mu \frac{h}{w})$ in equation (6), it introduces the following contribution in the momentum equation

$$\frac{1}{w} \mu p \frac{h}{\|\mathbf{D}\|} \operatorname{div}(\mathbf{D}) . \quad (23)$$

The viscous term remains identical since it is a function of $(\mu_2 - \mu_1)$.

This term is quite similar to the one in equation (22). It varies with the inverse of the width w and is proportional to μp . However, in the case of (23), the extra friction develops in the direction of the divergence of the strain-rate \mathbf{D} , scaled by the thickness of the flowing layer h divided by the shear-rate $\dot{\gamma} = \|\mathbf{D}\|$. In the present case, the term (22) acts in the direction of the velocity \mathbf{u} . It is important to point out that our approach leads to a non-linear correction that depends on the velocity unknown whereas the simpler approach linearly modifies the problem (by just increasing the internal friction coefficient). It consequently slows the motion (by changing the position of the static-flowing interface) but without modifying the velocity field. For instance, it would not be effective in a plane shear flow (more generally whenever the divergence of the deviatoric stress is zero). On the contrary, the extra friction introduced by (22) adds a contribution to the velocity field that non linearly counteracts the downslope flow and modifies the shape of the static-flowing interface and of the velocity field (see Section VII). It is thus active whenever a motion occurs.

Details of the numerical algorithm that implements the solution to the problem with lateral friction effect are given in Appendix A.

VI. EXPERIMENTAL SETUP

We briefly describe in this section the experimental setup used in Mangeney et al.²⁷ and Farin et al.⁹ that is being reproduced numerically in the present work (see also Ionescu et al.¹⁸).

It consists of a channel of rectangular section with plexiglas walls and a variable spacing w ($w = 10$ cm and $w = 20$ cm are considered hereafter). A mass of glass beads of height $h_0 = 14$ cm and of length $l_0 = 20$ cm

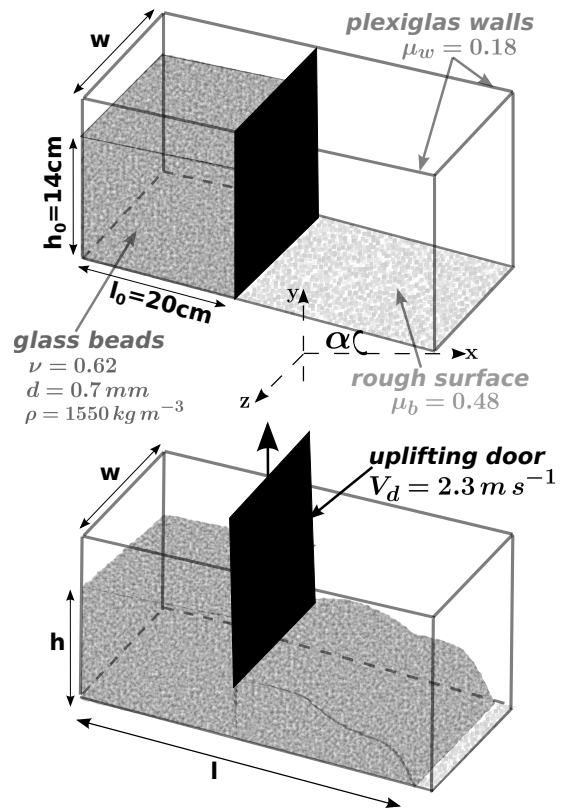


Figure 2. Sketch of the experimental setup

Table I. Rheological parameters

μ_1	μ_2	μ_b	μ_w	I_0	k
0.48	0.73	0.48	0.18	0.279	$0.035 \text{ kg}^{1/2} \text{ m}^{-1/2}$

is released from a reservoir at time $t = 0$ s by lifting a door. The glass beads are subspherical, cohesionless and highly rigid with a diameter $d = 0.7 \pm 0.1$ mm. They flow down an inclined surface of inclination α roughened with one glued layer of the same glass beads (see Figure 2). The particle density is $\rho_s = 2500 \text{ kg m}^{-3}$ and the volume fraction is estimated at $\nu = 0.62$ giving an apparent density $\rho = 1550 \text{ kg m}^{-3}$.

The thickness profiles of the granular mass are being recorded at various instants during the flow. The uplift of the door is simulated hereafter as a rigid boundary with a free-slip condition lifting at a velocity $V_d = 2.3 \text{ m s}^{-1}$ (see Ionescu et al.¹⁸ for details on the effect of the door on the flow).

The various rheological parameters are identical to those used in Ionescu et al.¹⁸ and are summarized in Table I. At the bed, $\mu = \mu_b$ is the basal friction coefficient and along the wall at the back of the reservoir and on the lateral walls, $\mu = \mu_w$ is the wall friction coefficient (see Figure 2).

VII. LATERAL WALL EFFECTS

This sections presents the results computed from the numerical model presented herebefore for different angles of the channel ranging from $\alpha = 0^\circ$ to $\alpha = 22^\circ$. A specific attention is paid to the improvement provided by the introduction of lateral friction effects, particularly at large slopes (typically $\alpha \geq 16^\circ$) where, as already mentioned, their absence has proved to be a strong limitation (see Ionescu et al.¹⁸). In the present formulation, the case without lateral friction effects is simulated using a large value for the width w (see equation (21)).

Two sets of experimental results are being used for comparison. The first one is the one presented in Mangeney et al.²⁷ that uses an experimental channel with a width $w = 10\text{cm}$ width. The second one is presented in Farin et al.⁹ and uses an experimental channel with a width $w = 20\text{cm}$. For both experiments, the initial granular column is rectangular, 20cm long and 14cm high (see Figure 2) leading to volumes of 2800cm^3 and 5600cm^3 respectively.

First, we compare the observed and computed thickness profiles of the granular material for different slopes α and both channel widths. Figure 3 and 4 represent, at different instants of the collapse, the observed and computed thickness profiles and the computed static flowing transitions on a 10° slope for $w = 10\text{cm}$ and $w = 20\text{cm}$ respectively. Figure 5 and 6 on the one hand, and Figure 7 and 8 on the other hand, plot the same results for $\alpha = 16^\circ$ and $\alpha = 22^\circ$ respectively.

The thickness profiles computed without lateral friction, corresponding to the former results presented in Ionescu et al.¹⁸ are plotted on every figure to highlight the (positive) effects of the lateral friction term.

The static-flowing transition is obtained as the isocontour for a velocity equal to 0.01 m s^{-1} . On Figure 3-8, the latest plotted instant corresponds to the observed (experimental) final time for the collapse.

A first observation is that the effect of the lateral friction term (see equation (21)) is more significant at large slopes (here 16° and 22°) than at small slopes (here 10°). This result make sense since the effect of the Coulomb friction arises only in the flowing zone and this flowing zone represents a larger part of the whole fluid domain when the slope increases. It follows that the area of the domain that is subject to lateral friction is bigger for an identical volume of flowing material.

This observation is consistent with the previous study of Ionescu et al.¹⁸ who showed that the ability to achieve a good prediction was deteriorating with an increased slope leading to the necessity to account for lateral friction effects.

Another general observation on the shape of the computed thickness profiles is the presence, particularly for $\alpha \geq 16^\circ$, of a slight yet systematic lowering of the surface in the upper-left corner. This shape is a numerical artifact related to the remeshing method and disappears for more refined meshes.

A. Final deposits

The computed final deposits are significantly improved by including lateral friction. The surface shape of the final deposit computed with lateral friction has a greater slope in average. The concavities and convexities of the surface are more pronounced leading to a better agreement with the experimental profiles.

This observation is true regardless of the width of the channel ; for $w = 20\text{ cm}$, the lateral frictional effects are smaller than for $w = 10\text{ cm}$ but remains clearly observable and significantly improve the numerical results.

For $\alpha = 10^\circ$ (Figure 3(d) and 4(d)), the static-flowing transitions show that the flow has clearly stopped and only very small areas of non-zero velocity close to the surface remain but too small to lead to any observable mass transfer. The extents of the final deposits are very accurate for both cases ($w = 10\text{cm}$ and $w = 20\text{cm}$), but not particularly improved compared to the case $w = \infty$. However, lateral friction term provided a small yet clear improvement of the computed shape of the surface (obviously more significant for $w = 10\text{cm}$).

For $\alpha = 16^\circ$ (Figure 5(d) and 6(d)), the shapes of the final deposits are again significantly improved. This time, we also observe that the extent of the final deposits is much more accurate when including the lateral friction. The runout distance computed without lateral friction is too big. The static-flowing transitions show that the numerical propagation has almost stopped for both cases. The remaining non-zero velocities do not affect the plotted final deposit. A small area of non-zero velocity can be seen at the front for the simulation without lateral friction effects but the velocity is small enough and does not induce any extra propagation after the plotted time.

For $\alpha = 22^\circ$ (Figure 7(d) and 8(d)), the differences are large. The extent of the deposit simulated without lateral friction is too long whereas the one with lateral friction remains very close to the observed one. As we can see from the static-flowing transition, in the simulation with lateral friction, there is still some velocity at the front but again too small to produce any significant extra propagation (smaller than 0.5%

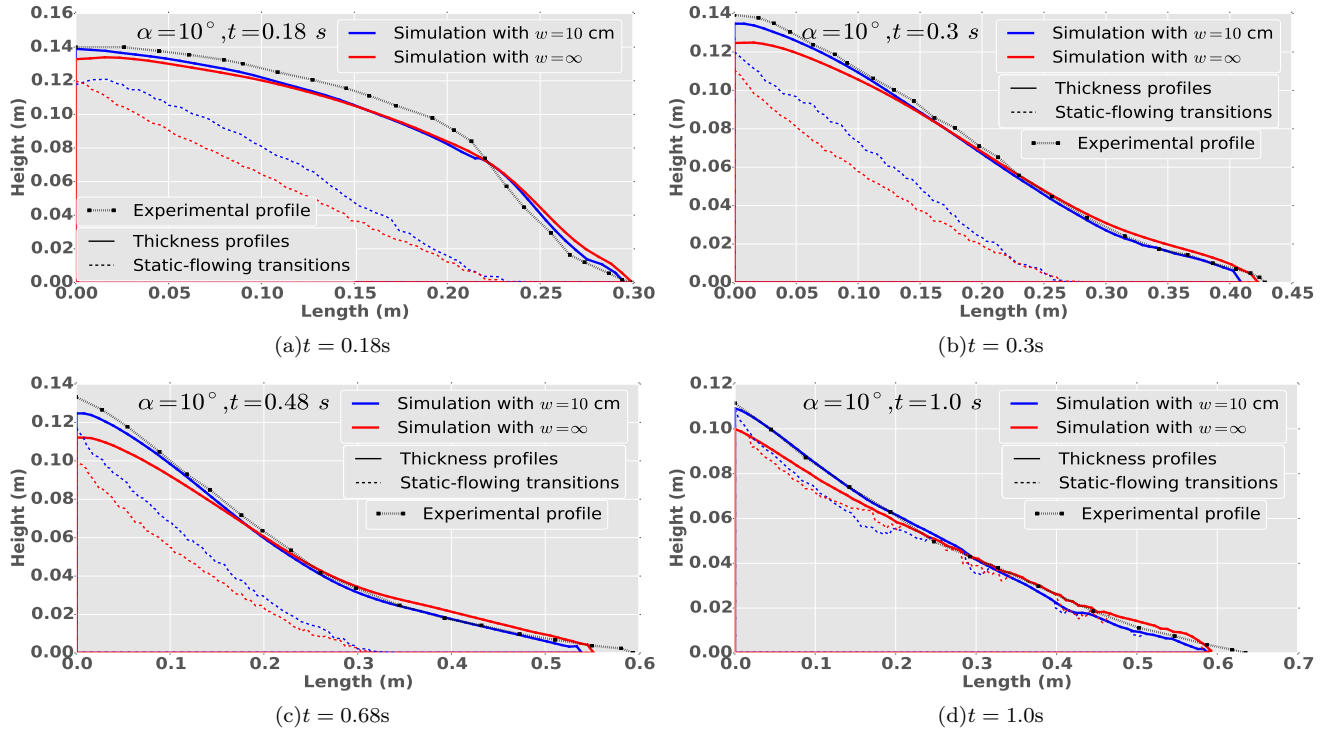


Figure 3. Computed and experimental thickness profiles for an inclination of the channel $\alpha = 10^\circ$ computed with the $\mu(I)$ rheology with and without lateral friction effects for $w = 10$ cm and corresponding computed static-flowing transitions. The axes scales are different for each time and the aspect ratio is thus not preserved.

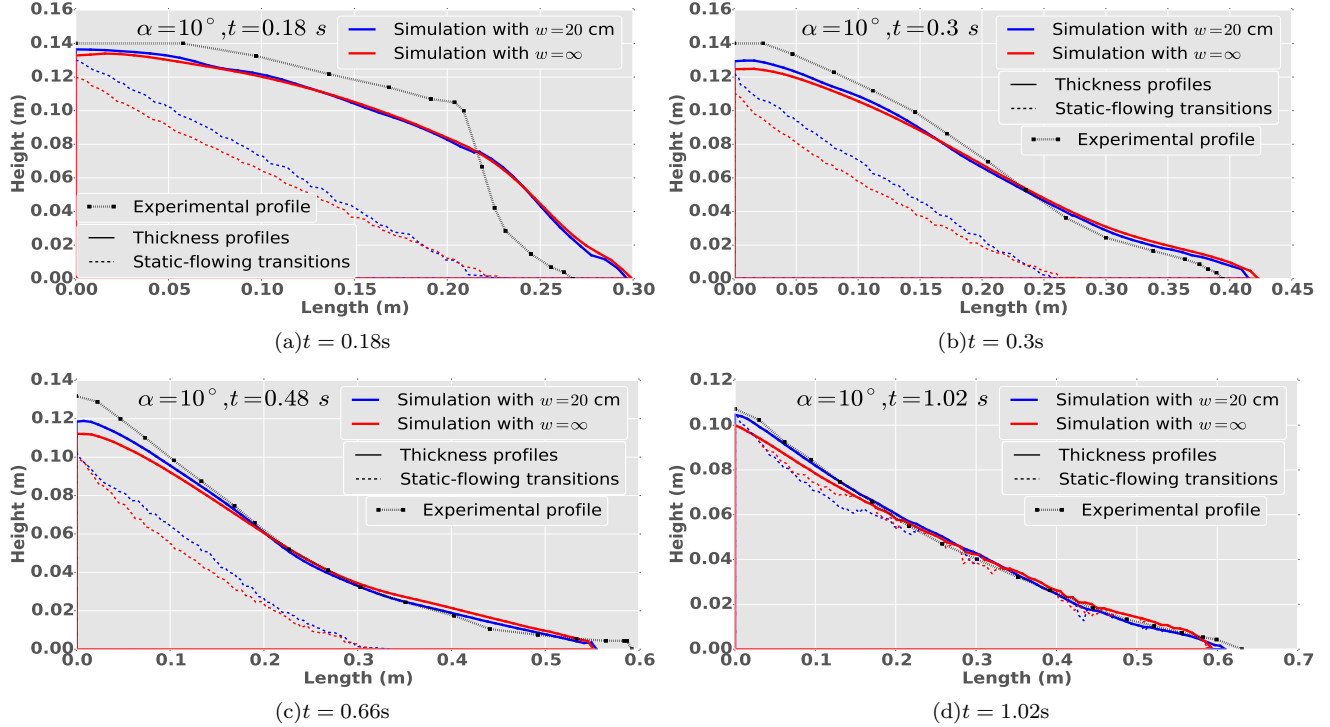


Figure 4. Computed and experimental thickness profiles for an inclination of the channel $\alpha = 10^\circ$ computed with the $\mu(I)$ rheology with and without lateral friction effects for $w = 20$ cm and corresponding computed static-flowing transitions. The axes scales are different for each time and the aspect ratio is thus not preserved.

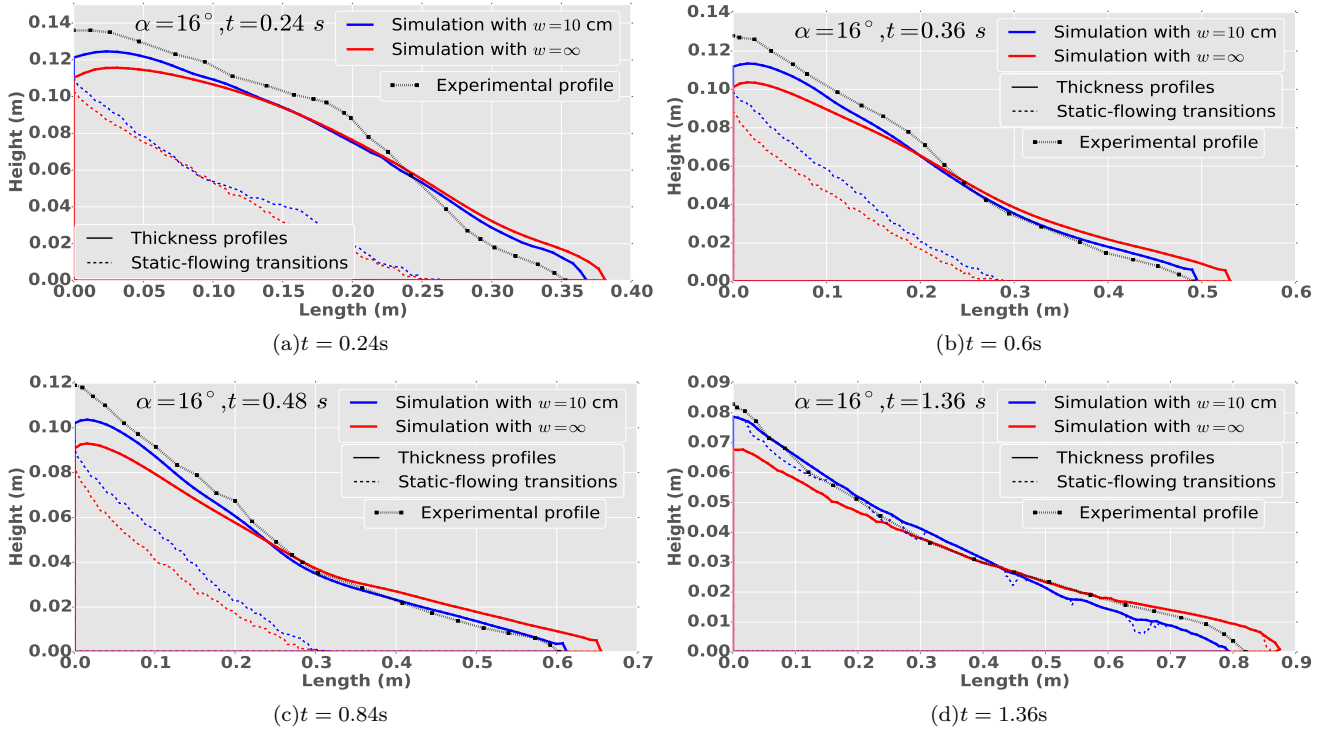


Figure 5. Computed and experimental thickness profiles for an inclination of the channel $\alpha = 16^\circ$ computed with the $\mu(I)$ rheology with and without lateral friction effects for $w = 10\text{ cm}$ and corresponding computed static-flowing transitions. The axes scales are different for each time and the aspect ratio is thus not preserved.

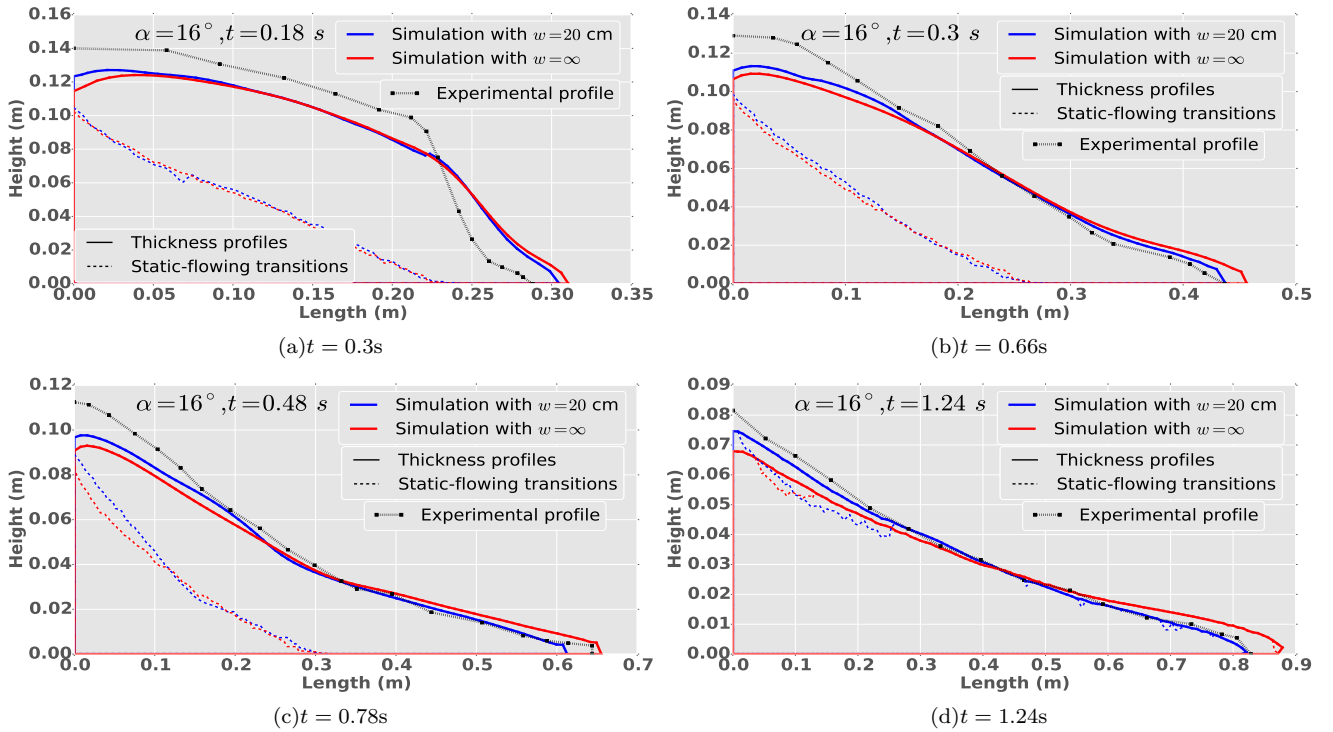


Figure 6. Computed and experimental thickness profiles for an inclination of the channel $\alpha = 16^\circ$ computed with the $\mu(I)$ rheology with and without lateral friction effects for $w = 20\text{ cm}$ and corresponding computed static-flowing transitions.

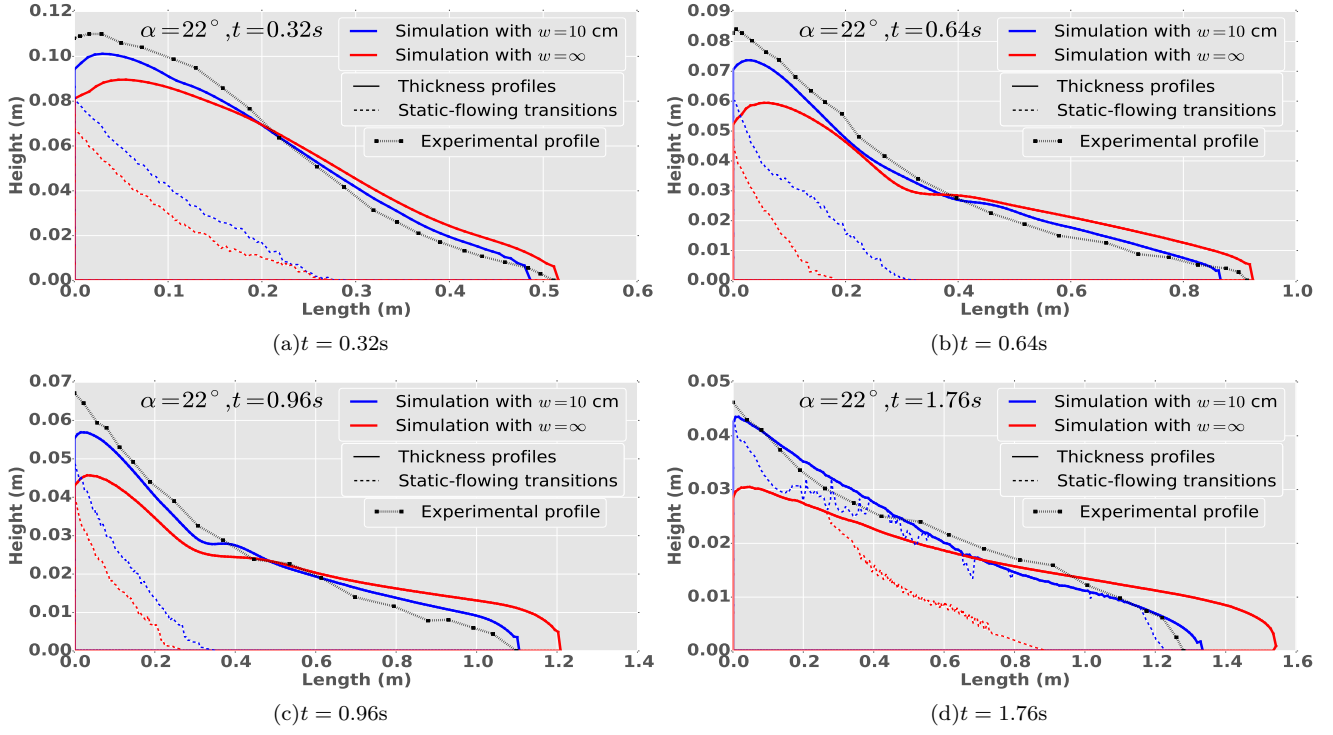


Figure 7. Computed and experimental thickness profiles for an inclination of the channel $\alpha = 22^\circ$ computed with the $\mu(I)$ rheology with and without lateral friction effects for $w = 10\text{cm}$ and corresponding computed static-flowing transitions. The axes scales are different for each time and the aspect ratio is thus not preserved.

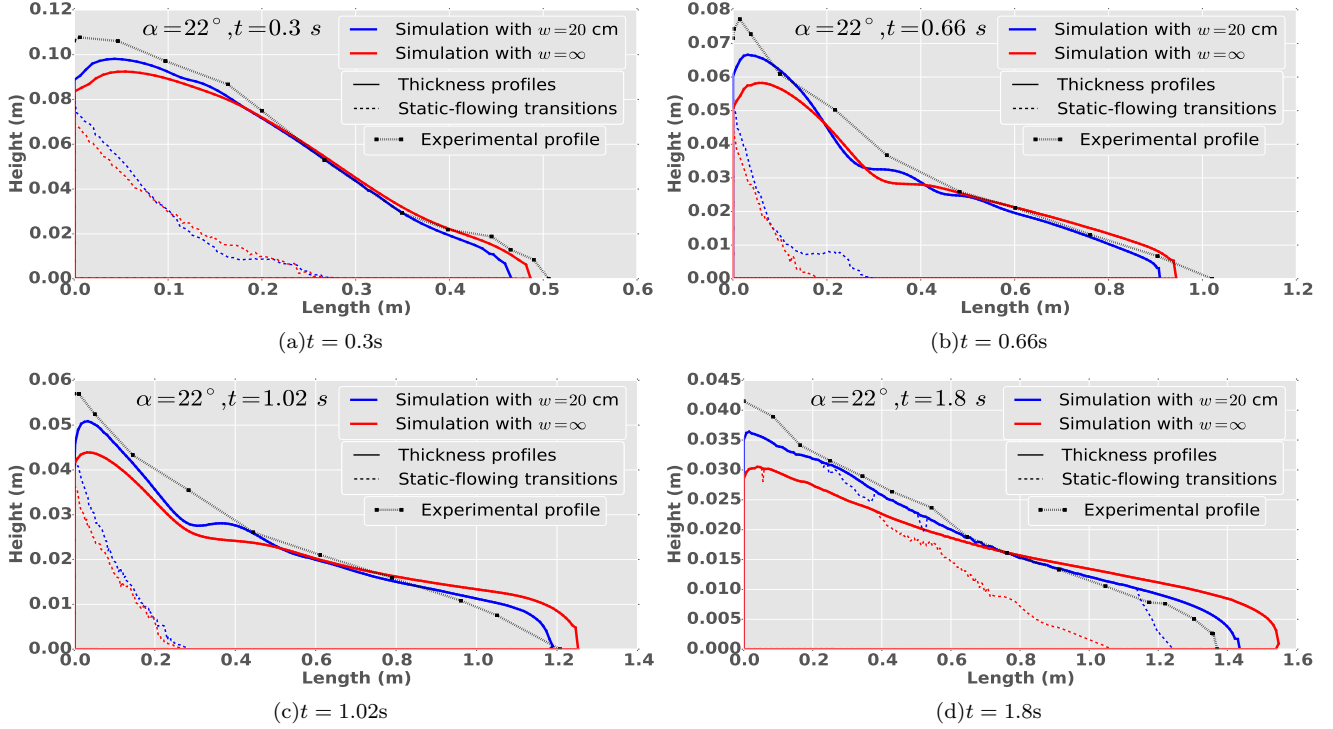


Figure 8. Computed and experimental thickness profiles for an inclination of the channel $\alpha = 22^\circ$ computed with the $\mu(I)$ rheology with and without lateral friction effects for $w = 20\text{cm}$ and corresponding computed static-flowing transitions. The axes scales are different for each time and the aspect ratio is thus not preserved.

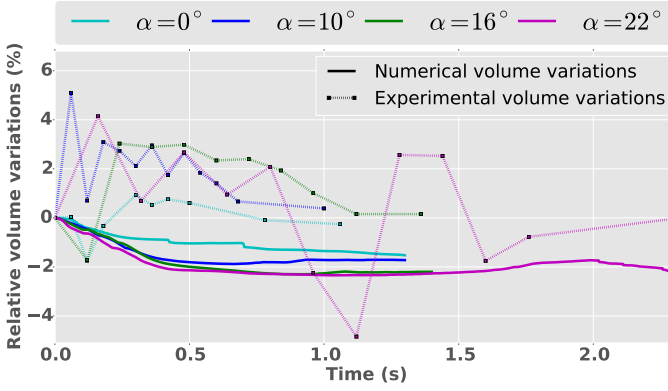


Figure 9. Volume variations during time in the experiments and the numerical simulations for $w = 10\text{cm}$ for inclinations of the channel $\alpha = 10^\circ$, 16° and 22° .

of the plotted runout distance). On the contrary, the simulation without lateral friction shows a large flowing area that will continue to transfer mass downstream and the computed runout distance reaches 1.6m.

B. Dynamical thickness profiles

The plotting of the static-flowing transitions allows to see the effect of the lateral friction term. In every cases, the lateral friction leads to a more convex transition (in the sense that the angle between the static-flowing interface and the bottom of the channel is greater) that prevents mass from the upper-left corner to flow downstream. It makes sense since the lateral friction term acts only on the flowing part and in the direction of the flow.

Thus, the surface remains more convexe along the collapse and that clearly reflects more accurately the experiments. In every cases, the earlier instant (Figures 3(a)-4(a), 5(a)-6(a) and 7(a)-8(a)) is the less accurate. A first reason is that even though the simulation models the presence of the uplifting door, it considers a free-slip boundary condition on it and the experiments clearly shows (see Ionescu et al.¹⁸) a frictional effect of the uplifting door that perturbs the flow at the beginning. We point out that the plots does not have the same scale on the horizontal and the vertical axis (because the aspect ratio of the plotted domain goes from almost 1 up to 50), thus (possibly strongly) enhancing the horizontal variations of the surface.

The other aspect is the strong dilatancy effects that occurs in the experiments. Figure 9 and 10 plot the variation of volume as a function of time for the numerical simulation and the experiments in both channels ($w = 10\text{ cm}$ and $w = 20\text{ cm}$).

As we can see, the typical experimental behavior is

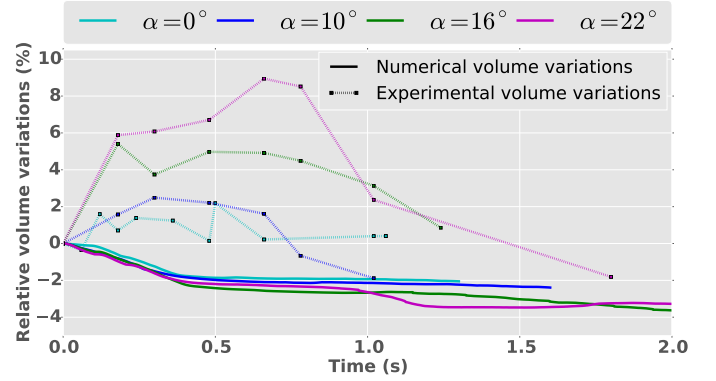


Figure 10. Volume variations during time in the experiments and the numerical simulations for $w = 20\text{cm}$ for inclinations of the channel $\alpha = 10^\circ$, 16° and 22° .

an important volume increase at the beginning that decreases after some time to approximately retrieve the original compaction. In the case $w = 10\text{ cm}$ (Figure 9), the experimental volume generally exhibits less than 3% of volume variation but locally reaches up to 5% of dilatancy (and compaction for $\alpha = 22^\circ$). In every case, the final volume is almost equal to the initial one. These variations in volume partly explain the difficulty for the incompressible numerical simulation to reproduce the transient state with the same accuracy as the final one, especially since the numerical simulation tends to lose mass (around 2% at the end) when the domain quickly evolves (so basically during the acceleration phase). This numerical mass loss appears to be bigger on larger slopes. This observation suggests that an adaptive time scheme would be relevant to perform smaller time steps in the acceleration phase. We point out that another possibility for reducing mass loss is to consider a higher refinement of the mesh. We observed that the numerical mass loss behaves linearly with the refining of the mesh (typically for a mesh size twice as small, the numerical mass loss is divided by 4).

In the case $w = 20\text{ cm}$ (Figure 10), the variations of volume are stronger, and strictly increase with the slope. For $\alpha = 22^\circ$, the volume increase is close to 10%. In addition, the volume of the final deposit is less close to the initial one than in the case $w = 10\text{ cm}$ and, in the case $\alpha = 22^\circ$, more compact (but this might be due to experimental measurement errors). Conversely, the numerical mass behaves rather identically to the case $w = 10\text{ cm}$. The velocities being slightly higher when $w = 20\text{cm}$, the mass loss seems to be slightly higher too but remains smaller than 3%.

It is important to note that the use of a broader channel for the experiments, while providing reduced lateral wall effects, also allows for a stronger dilatancy to occur.

In any case, a more accurate prediction of this type of experiment could only be achieved through the modeling of the dilatancy effects for instance through a dilatant Drucker-Prager model that takes into account the evolution of the volumic fraction with respect to the shearing of the material (see *e.g.* Andreotti et al.²).

The extents of the collapsing mass at intermediate times are pretty accurate and globally improved by including lateral friction. The very end of the mass (*i.e.* close to the front) is not always sharply determined but this effect is mainly due to the size of the mesh cells compared to the aspect ratio of the domain (which goes from approximately 1 at the beginning up to 50 for the final deposit at $\alpha = 22^\circ$). A higher refinement of the mesh would have produced a better description of the front zone. In other respect, the experimental measurement of the location of the front can be unreliable due to the saltation of the beads. It leads to an error on the runout distances estimated to 10% in general (see Farin et al.⁹).

From these aspects, it appears insufficient to compare only the thickness profiles since their precision is limited by the sharpness of the mesh, the variations of volume and the possibly variable precision of the experimental measurements. To take a closer look at the dynamical behavior, we consider in the next part the evolution of the velocities at the front during the collapse.

C. Front velocities

Figure 11 and 12 plot the computed velocities at the front of the fluid domain during the collapse with and without lateral friction. for $w = 10\text{cm}$ and $w = 20\text{cm}$ respectively. In order to compare, the experimental front velocities are also plotted. The experimental front velocities have not been directly measured and the resulting plot simply correspond to the finite rates of change (*i.e.* $\Delta x/\Delta t$) computed on the observed positions of the front. The curves consequently have few points with little precision about their position in time. However, it allows to observe the general behaviour.

It clearly appears that the experimental front velocities are closer to the velocities computed with lateral friction effects. Typically the maximum velocity reached for a given situation is better reflected when including lateral friction effect. At 22° , in both cases, the deceleration phase shows a much faster deceleration in the experimental measurements followed by a change of slope. This behavior, designated by “slow propagation phase” (see Mangeney et al.²⁷, Farin et al.⁹), is not captured by the simulations, regardless of the lateral friction effects. As we show in Section VIII, this slow propagation phase is related to the rheology of the flow

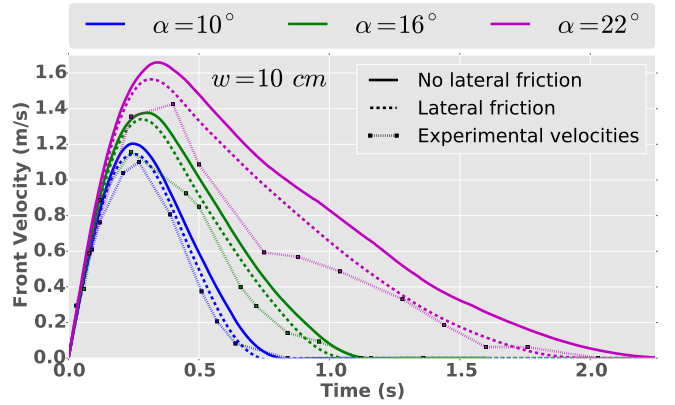


Figure 11. Velocity of the front as a function of time computed with and without the lateral friction term and experimental velocities (obtained from the evolution of the position of the front with time) for $w = 10\text{cm}$ for inclinations of the channel $\alpha = 10^\circ$, 16° and 22° .

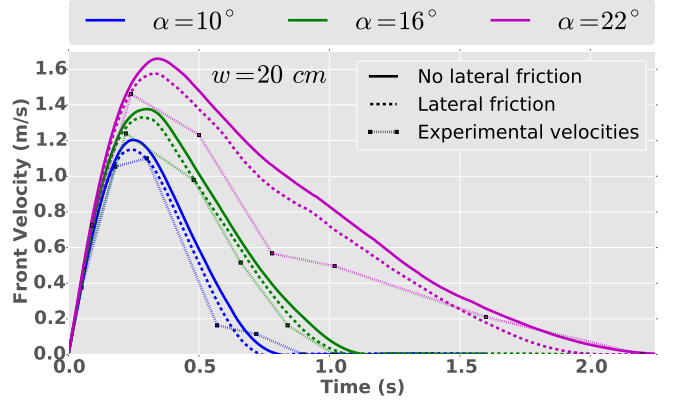


Figure 12. Velocity of the front as a function of time computed with and without the lateral friction term and experimental velocities (obtained from the evolution of the position of the front with time) for $w = 20\text{cm}$ for inclinations of the channel $\alpha = 10^\circ$, 16° and 22° .

and its parameters.

VIII. ROLE OF THE SPATIAL VARIABILITY OF THE VISCOSITY η_I IN THE $\mu(I)$ VISCOPLASTIC MODEL

A. Thickness profiles and front velocities

From equation (6) and (7), it is clear that the use of the $\mu(I)$ rheology leads to model a viscoplastic fluid with a yield stress depending on the pressure. In that sense, the $\mu(I)$ rheology is not very different from a viscoplastic fluid with a Drucker-Prager plasticity criterion, except for the spatially variable viscosity η_I (see equation (7) and (8)). The aim of this section is to determine more specifically the role of the spatial variability of η_I in the

viscoplastic model (see (8)). Many works (*e.g.* Lagree et al.²⁴, Andreotti et al.², Silbert et al.³⁶, Jop et al.¹⁹) has proved that a Newtonian model fails to predict a granular flow. We can safely assume that the viscoplasticity is then of primary importance to achieve a good modelization. However, until now, little attention has been paid to the role of the dependance of the viscosity η_I to the inertial number (except in Ionescu et al.¹⁸). In what follows, two different models are considered. The η_I model (see (8)) and the Drucker-Prager model where the viscosity η defined by (7) is taken constant: $\eta = \eta_c = 0.4$ Pa s. This value corresponds to a coarse global average of the range of values computed using η_I (see Figure 15).

Figure 13 plots the front velocities for various slopes computed with $\eta = \eta_I$ and $\eta = \eta_c$ (see equation (7) and (8)) considering an infinitely wide channel ($w = \infty$ in (21)). Figure 14 plots the same results with $w = 10$ cm.

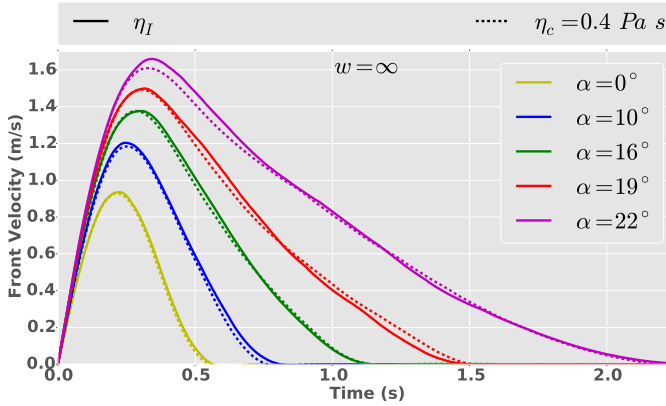


Figure 13. Velocity of the front as a function of time for $\alpha = 0^\circ, 10^\circ, 16^\circ, 19^\circ$ and 22° computed with η_I viscosity and constant viscosity $\eta_c = 0.4$ Pa s. The velocities have been computed without lateral friction effects ($w = \infty$).

In both cases ($w = \infty$ and $w = 10$ cm), the differences between η_I and η_c are small in both the acceleration phase and the deceleration phase, the maximum velocity and the stopping time. The key point is to observe that the behavior of the front velocities is preserved and the viscosity η_I does not predict any peculiar behavior that the constant viscosity model fails to predict. The observable differences only come from the fact that the value of $\eta = 0.4$ Pa s is slightly higher in general than the arithmetic average of the viscosity computed by equation (7) leading to a slightly slower flow.

As a matter of fact, not only the front velocities but also the dynamical shape of the domain is hardly affected by the variable viscosity. Figure 15 represents the contour of the domains computed with and without a variable viscosity, for different slopes, at the time corresponding to the maximum velocity where the inertial

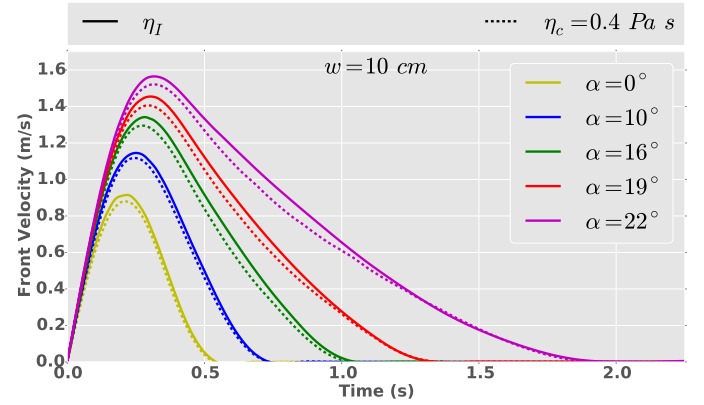


Figure 14. Velocity of the front along time for $\alpha = 0^\circ, 10^\circ, 16^\circ, 19^\circ$ and 22° computed with η_I viscosity and constant viscosity $\eta_c = 0.4$ Pa s. The value for the constant viscosity $\eta = 0.4$ Pa s is chosen as an average value of the viscosity obtained from equation (7) in the flowing part of the fluid domain. The velocities has been computed with $w = 10$ cm.

number strongly varies within the fluid domain (typically I varies between 10^{-3} close to the static-flowing transition to 1 at the surface and the front, see Ionescu et al.¹⁸).

As we can observe, the thickness profiles hardly differ from one another even if the viscosity field varies significantly within the domain. The low sensitivity of the model to the spatial variability of the viscosity has been highlighted for other non-Newtonian fluids (see *e.g.* Martin and Monnier²⁹). We retrieve the fact that the value of 0.4 Pa s is suited as a coarse average value of the viscosity η_I .

While the spatial variability of the viscosity does not have a significant influence on the flow, we observed that the absolute value of the viscosity has. We plot on Figure 16, for different slopes, the results obtained with η_I and η_c models for different constant values of η_c .

In the acceleration phase the behavior is almost preserved when changing the value of the viscosity. A high viscosity leads to a smaller maximum velocity. The slopes of the curves in the acceleration phase identical during the first part of the acceleration phase. They start to differ from one another before the velocity peak and the value $\eta_c = 1$ Pa s provide a better fit to the experimental velocities.

In the deceleration phase, the behavior is significantly modified by changing the value of η_c . It appears that the convexity of the curve is strongly related to the value of η_c . A smaller value leads to an almost constant deceleration whereas a higher value induces a change of slope in the velocity curve. The differences remain small at small slopes. For $\alpha = 22^\circ$, the value $\eta_c = 1$ Pa s predicts two different regimes in the deceleration

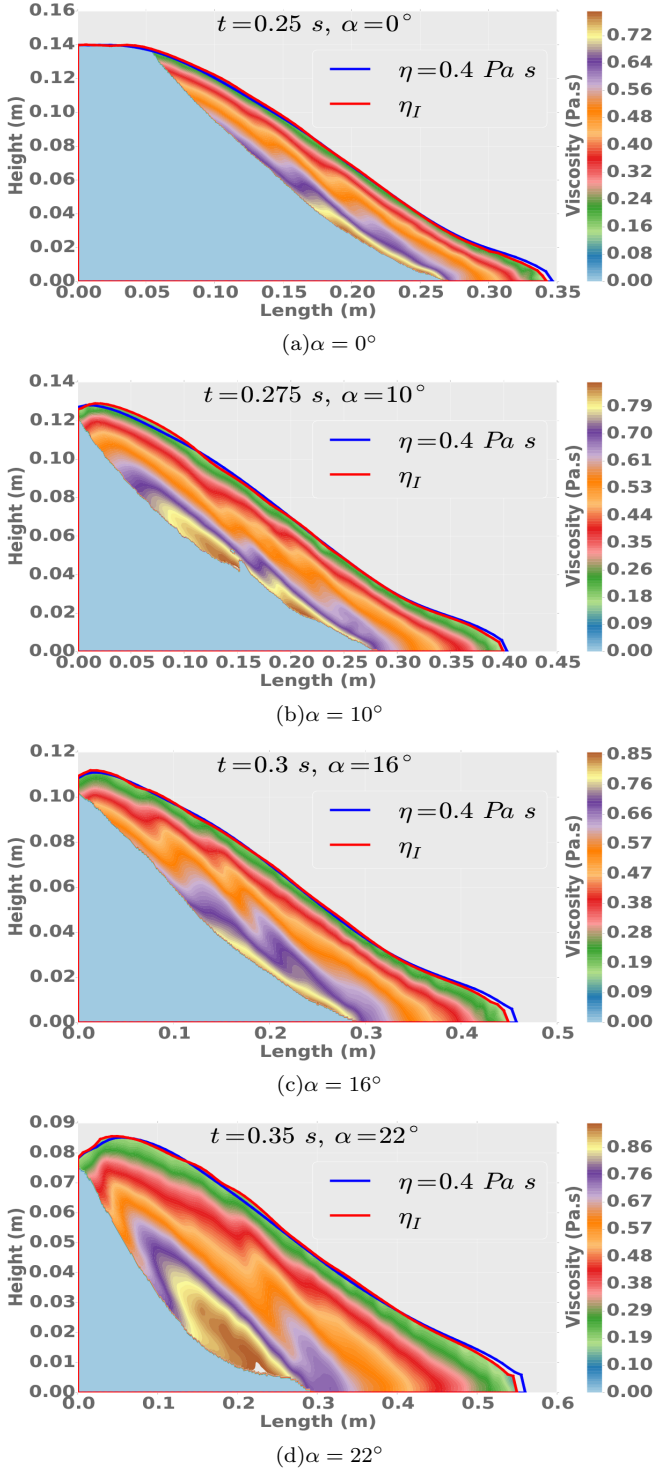


Figure 15. Computed thickness profiles for inclinations of the channel $\alpha = 0^\circ, 10^\circ, 16^\circ$ and 22° computed with η_I and η_c . The color field displays the value of the viscosity η_I in the flowing part (see (7)). The velocities have been computed with $w = 10\text{cm}$. The viscosity field in the static part has been set to 0 for clarity.

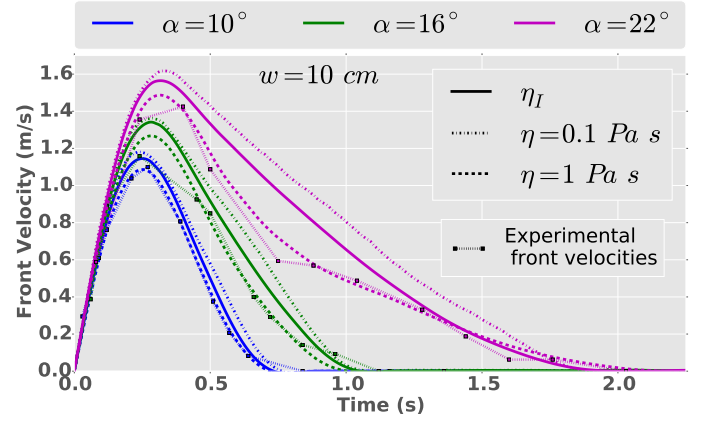


Figure 16. Computed and experimental velocities of the front as a function of time for $w = 10\text{cm}$ and for inclinations of the channel $\alpha = 10^\circ, 16^\circ$ and 22° computed with η_I and η_c . The values $\eta_c = 0.1\text{Pa.s}$ and $\eta_c = 1\text{Pa.s}$ has been chosen as the bounds of the viscosity range provided by η_I (see Figure 15).

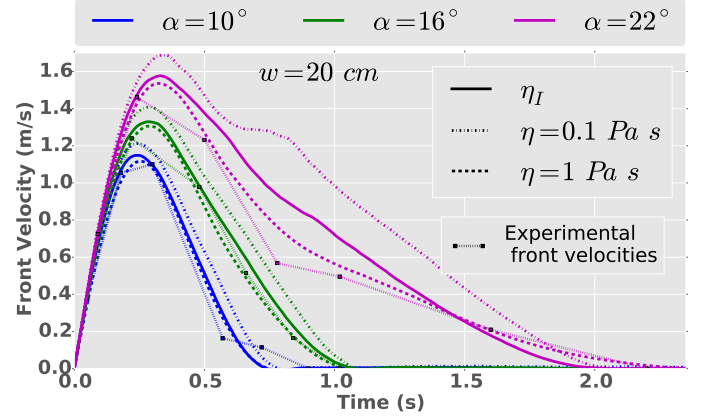


Figure 17. Computed and experimental velocities of the front as a function of time for $w = 20\text{cm}$ and for inclinations of the channel $\alpha = 10^\circ, 16^\circ$ and 22° computed with η_I and η_c . The values $\eta_c = 0.1\text{Pa.s}$ and $\eta_c = 1\text{Pa.s}$ has been chosen as the bounds of the viscosity range provided by η_I (see Figure 15)

phase: first a quick deceleration followed by what can be seen as a slow propagation phase. To highlight the slow propagation phenomenon, we plot on Figure 18 and 19 for $\alpha = 22^\circ$, for $w = 10\text{cm}$ and $w = 20\text{cm}$ respectively, the results obtained with η_I , $\eta_c = 1\text{Pa.s}$ and $\eta_c = 2\text{Pa.s}$.

As we can see, the slow propagation phenomenon in the case $\eta_c = 2\text{Pa.s}$ is stronger than for $\eta_c = 1\text{Pa.s}$, leading to a more significant change of slope in the deceleration phase. One can deduce that the slow propagation phase is related to the balance between the mean viscosity of the flow and the other adjustable physical quantities of the model, namely the (internal and boundary) friction coefficients. However, in that case, the value of the viscosity is too high and the

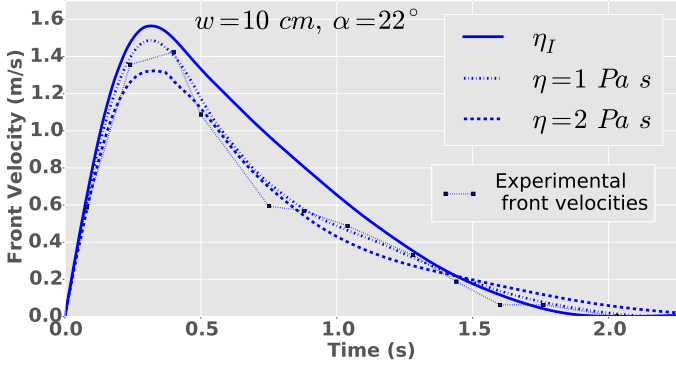


Figure 18. Computed and experimental velocities of the front as a function of time for $w = 10\text{cm}$ and for $\alpha = 22^\circ$ computed with η_I , $\eta_c = 1\text{Pa s}$ and $\eta_c = 2\text{Pa s}$.

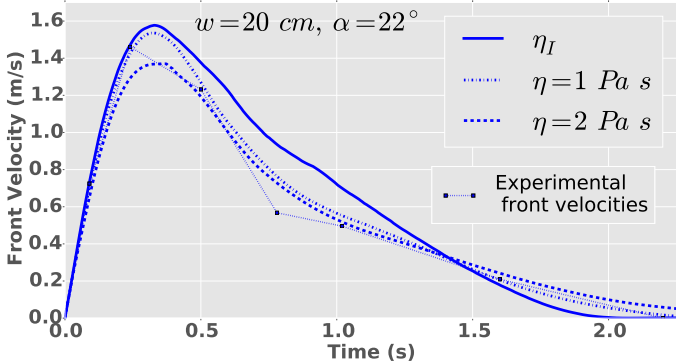


Figure 19. Computed and experimental velocities of the front as a function of time for $w = 20\text{cm}$ and for $\alpha = 22^\circ$ computed with η_I , $\eta_c = 1\text{Pa s}$ and $\eta_c = 2\text{Pa s}$.

computed velocities are too small compared to the experimental velocities.

This slow propagation phase has been clearly demonstrated by experimental measurements (see Farin et al.⁹, Mangeney et al.²⁷) mainly at high slopes. As a matter of fact, the curves obtained with $\eta_c = 1\text{Pa.s}$ much better agree with the experimental front velocities in all the phases of the flow (acceleration, deceleration, slow propagation) and for every angle. The very good agreement between the simulation with $\eta_c = 1\text{Pa s}$ and the experimental front velocities allows to notice that the maximum velocity does not appear on the experimental points.

B. Pressure fields

A classical simplification of these granular flows, typically for large scale realistic simulations, is to consider the pressure to be hydrostatic in the flow. However, the pressure within a Drucker-Prager flow is a priori different

from the hydrostatic pressure. Recent works (Bouchut et al.⁴) have proposed, under some assumptions, terms of correction for the pressure field from a shallow-type model, in order to include the effects deviating from the hydrostatic pressure. The resulting second order analytical pressure is derived from the Drucker-Prager model with constant viscosity η_c . It is written in the topography related frame (X, Z) :

$$p = \rho g \left(\cos(\alpha) + \sin(\alpha) \partial_X h - 2 |\sin(\alpha)| \frac{\partial_X U}{|\partial_Y U|} \right) (h - Y) + \mathcal{O}(\varepsilon^3) \quad (24)$$

where (U, W) is the velocity field and $h(X)$ is the height of the free-surface (in the topography related frame (X, Z)). We point out that this analytical pressure is derived under a shallow-type approximation (thickness, stresses and pressure of order ε) combined with a slow flow approximation (streamwise velocity of order ε). There are two extra terms (deviating from the hydrostatic pressure component) that includes a surface slope effect and a streamwise velocity gradients related component. It implies that this pressure is only defined in the flowing phase. The expression of (24) in the gravity related frame (x, z) considered hereafter is given in Appendix B.

In order to look further into the effect of the spatially varying viscosity η_I , we compare hereafter the computed pressure profiles on a slope $\alpha = 22^\circ$ obtained with η_I and η_c to the analytical pressure given in (24). Because of the model hypothesis, we consider the results at time $t = 1.5\text{s}$, in order to have a rather shallow problem with a relatively small average velocity (consistently with the hypothesis of the analytical pressure). The domain is plotted on Figure 20. The resulting pressure profiles are plotted on Figure 21.

We point out that the free-surface of the domain computed with η_I (see Figure 20) presents a perturbed aspect whereas the one computed with η_c smoothly varies. As a matter of fact, it is a systematic behavior and the most observable effect of the variable viscosity η_I , conversely to the constant one.

A first observation is that the analytical pressure significantly improves the hydrostatic approximation and allows to capture quite well the pressure variation with depth that deviates from the hydrostatic pressure. Since the fluid domains computed with η_c and η_I are slightly different, obviously the pressure profiles at a given abscissa x are different. However, they are quite similar for every x .

Regarding the comparison between η_I and η_c , we can see that the analytical pressure (24), derived from the constant viscosity Drucker-Prager model, allows, with an identical precision, to describe the pressure

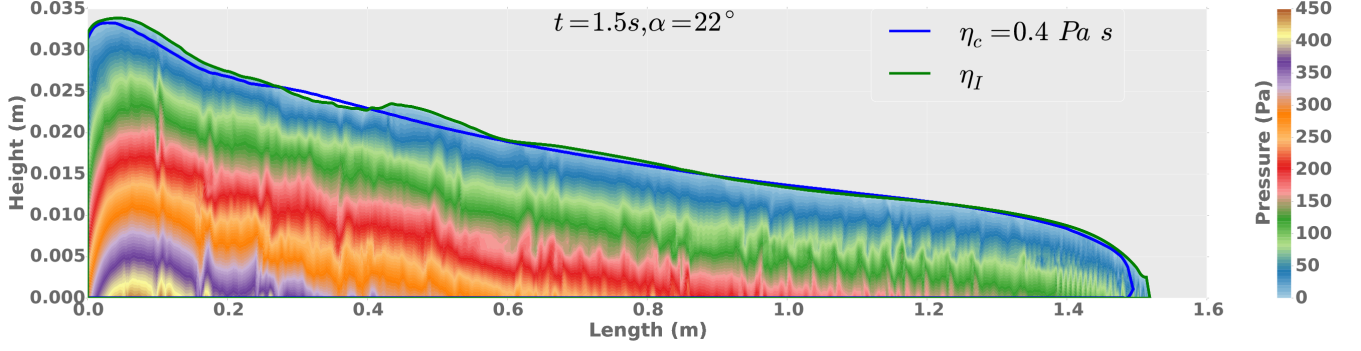


Figure 20. Thickness profiles of the granular collapse computed for $\alpha = 22^\circ$ with variable η_I and constant η_c at $t = 1.5\text{s}$. The colored surface represent the pressure field computed with η_I . It is worth noting that the real aspect ratio of the plot is a tenth as small as the plotted one (hence the perturbed aspect of the pressure field).

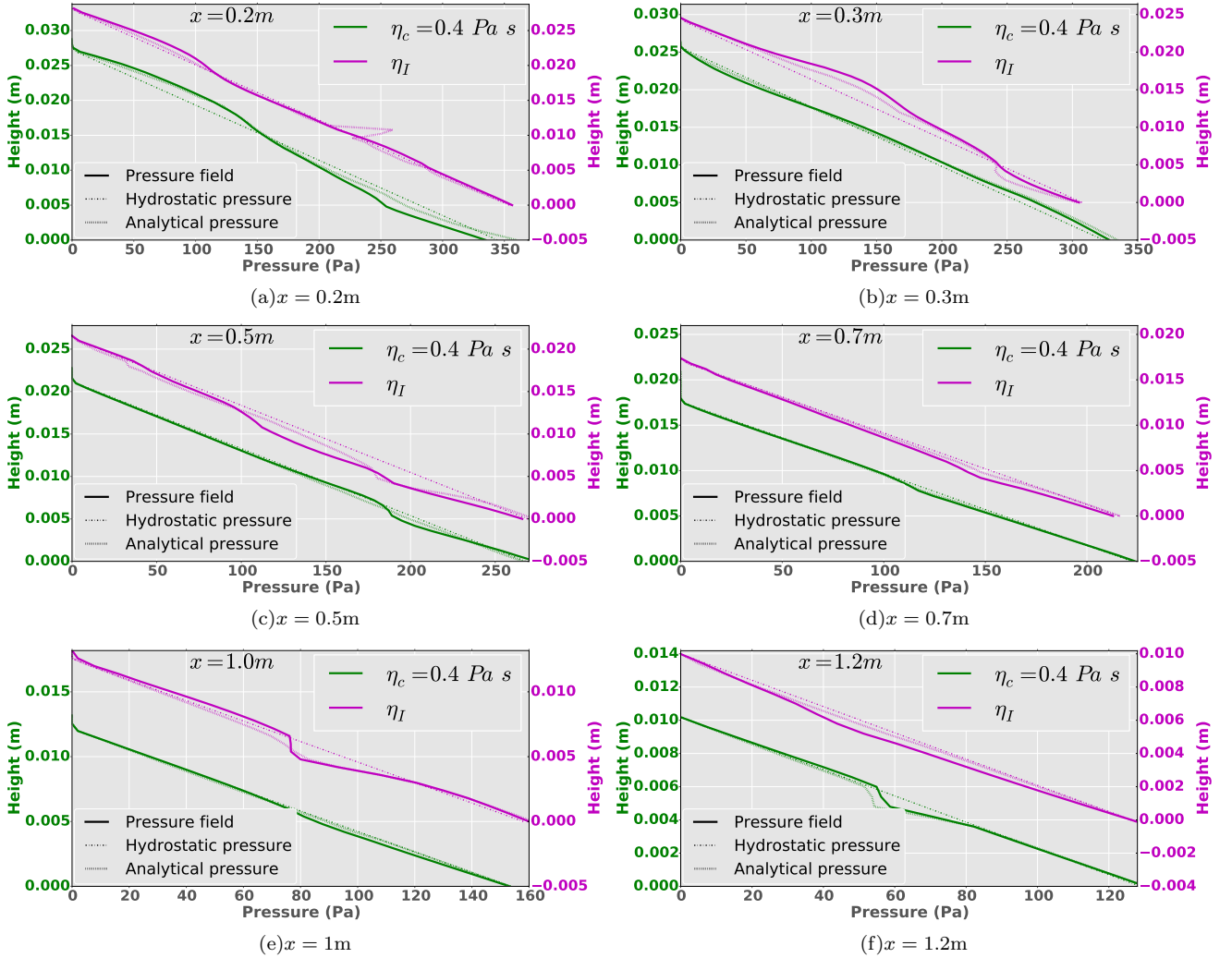


Figure 21. Pressure profiles at different abscissae extracted from the pressure field computed with η_I and plotted on Figure 20 and its counterpart computed with η_c , analytical pressure evaluated from (24) and corresponding hydrostatic pressure. The profiles in magenta are plotted using the right y-axis. The plotted profiles are vertical cuts of the domain plotted on Figure 20.

field computed with and without the varying viscosity η_I .

It results that the η_I viscosity does not seem to influence the model in terms of pressure as the pressure field is hardly affected by this variable viscosity and the analytical pressure that does not take into account this viscosity variability in space is able to predict the pressure variations of the model solved with η_I .

C. Summary

In the present case, we have seen that the variable viscosity η_I induced by the $\mu(I)$ rheology is of very little effect when compared to a constant viscosity model with the same value of viscosity in average. But we have also demonstrated that the value of viscosity η_I , based on physical quantities, is not exactly suited; indeed, a constant viscosity model with a value chosen in the limits of the η_I viscosity range significantly improves the simulations and allows to capture the slow propagation phase.

Theses results assess the fact that the $\mu(I)$ rheology is mainly efficient because it transforms the classical plastic model to a Drucker-Prager viscoplastic model. The dependency of the viscosity to the inertial number allows to provide, from physical quantities, an idea of the correct value of the viscosity. In the present case, however, the resulting value is too small.

In any case, a computation with the variable viscosity η_I induces a higher computational burden and a slower convergence that can lead to overall simulations twice as long, in the present case.

IX. SHEARING INSTABILITIES

This section focuses on the presence of confined zones of high shearing, that can be seen as shear bands, which appears systematically in the simulations. We show that this result cannot be captured by refining the mesh and is consequently related to an instability-type phenomenon. However, the simulations show that this instability does not affect the result in terms of dynamical shape of the computational domain and that it is triggered by the coupling of the plasticity criterion with the solution through the pressure-dependency.

We first plot on Figure 22 the norm and isocontours of the computed velocity field and the corresponding shear-rate field at time $t = 0.1s$ on a 0° slope for mesh sizes $h = 0.008m$, $h = 0.004m$ and $h = 0.002m$ (corresponding to approximately 1000, 5000 and 20000 triangular cells). As we can see on the coarser mesh (Figure 22(a)), the isolines are basically evenly spaced

according to the value of the velocity field. As we refine the mesh, the velocity field becomes stratified and bands of high gradient in the velocity field appear. On the finer mesh, the phenomenon is very clear and the velocity field almost appear as a sequence of plug flows separated by thin zone of high gradient. This behavior is clearly retrieved on the shear-rate field (Figure 22(d)-22(f)), and what can be called shear bands appears at the interfaces between the plug zones.

This behavior is not stable since there is no convergence of the computation to a given number of shear bands when mesh size decreases, from the best of our refining capacities; the shear bands always covering a thickness of two to three elements, which is the smallest size for a phenomenon to be captured by a discrete computation. The highest refinement we have been able to reach was predicting bands as narrow as 4 grain diameter.

However, this mesh dependent phenomenon does not affect the stability of the simulation. First, we can see that the velocity range is not affected by the shear bands and only its spatial structure is. As a matter of fact, in a more global point of view, we can observe that the stability of the computational domain movement is preserved.

Figure 23 plots the thickness profiles of the same simulation ($\alpha = 0^\circ$) at time $t = 0.5s$ for the three mesh sizes. From this figure, we clearly observe that the thickness profiles are not modified when refining the mesh and the differences that can be observed between the three profiles are completely expected regarding the higher precision one gets from a finer mesh.

The results plotted on Figure 22 have been computed using a constant viscosity $\eta = 0.4Pa.s$ without lateral friction effects. We point out that the use of a $\mu(I)$ viscosity and/or lateral friction does not change this result.

To understand what triggers this effect, the same problem is solved for different plasticity criterions. Figure 24 plots the results for the 3 mesh sizes in the case of a constant yield stress $\kappa = 100$ (see equation (1)) and a constant viscosity $\eta = \eta_c$, thus leading to a Bingham fluid.

This time, no such shearing bands appear. The refining of the mesh leads normally converging velocity and shear-rate fields. This result highlights the fact that the shear bands effect is related to the coupling of the plasticity criterion with the pressure field. This coupling has two different aspects. On the one hand it induces a coupling of the plasticity criterion with the solution to the momentum problem which can be seen as a strong coupling, and on the other hand, since it varies spatially, it couples the criterion with the geometry of the problem

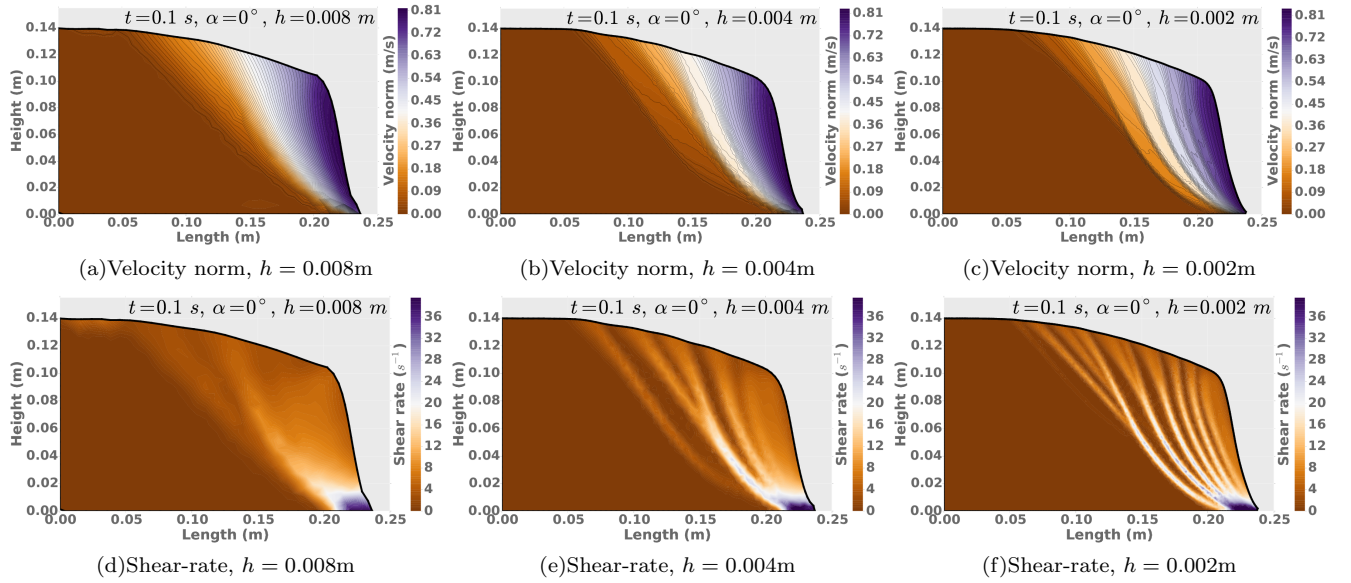


Figure 22. Velocity norm and shear-rate computed at time $t = 0.1s$ on a slope $\alpha = 0^\circ$ on meshes with cells of size h for the Drucker-Prager problem with constant viscosity. The colorscale of the plots of the shear-rates has been saturated for the sake of readability to a maximum shear-rate of $40s^{-1}$

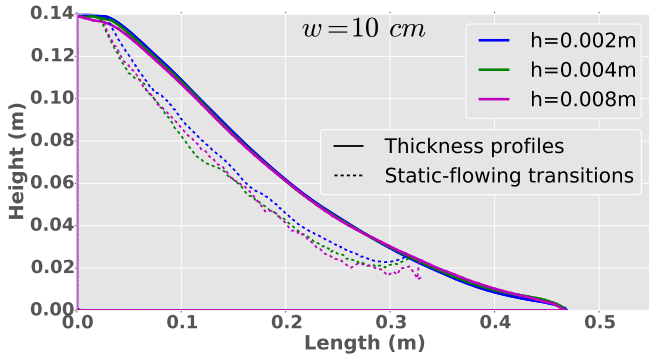


Figure 23. Thickness profiles computed with increasingly fine meshes at time $t = 0.5s$ on a 0° channel and the corresponding static-flowing transitions.

which is a weaker coupling.

In order to separate these effects, we consider this time a plasticity criterion taken equal to the hydrostatic pressure at each time step, thus resulting in a weak geometrical coupling of the plasticity criterion with the free-surface. Since the hydrostatic pressure sharply varies within an almost rectangular domain, these simulations have been performed starting from a trapezoidal column (inspired from the one considered in Farin et al.⁹). We plot on Figure 25 the results at time $t = 0.1s$ on the three meshes.

In this case, the computations again appear to be converging with the refining of the mesh. The velocity field structure is preserved when refining and the shear-

rates also show the convergence of the spatial structure. For instance, the presence of a trapezoidal patch of high shear close to the lower-right corner is nicely captured.

From these results, we have clearly established that the shear bands effect is directly triggered by the coupling of the plasticity criterion with the solution of the problem through its pressure dependency. Based on the different results, this phenomenon does not appear to be a numerical instability (simulations of the collapse are accurate, stable in time when refining and the choice of other types of plasticity criterion leads converged solution devoid of instabilities). It follows that this phenomenon seems to be inherent to the Drucker-Prager viscoplastic model.

X. CONCLUSION

FL modifie la forme de l'écoulement contrairement a $\mu+0.1$. A forte pente, avant ca marchait pas, maintenant ca marche. This result is all the more significant that realistic geophysical granular flows mostly occur on large slopes.

Rappeler les resultats sur la dilatation (et le fait qu un canal plus large c bien et pas bien).

The ability for the model to capture the slow propagation phase is an important aspect of validating the underlying physics of the equations. In the present case, we thus see that a constant viscosity Drucker-Prager model is able to produce it whereas the variable viscosity

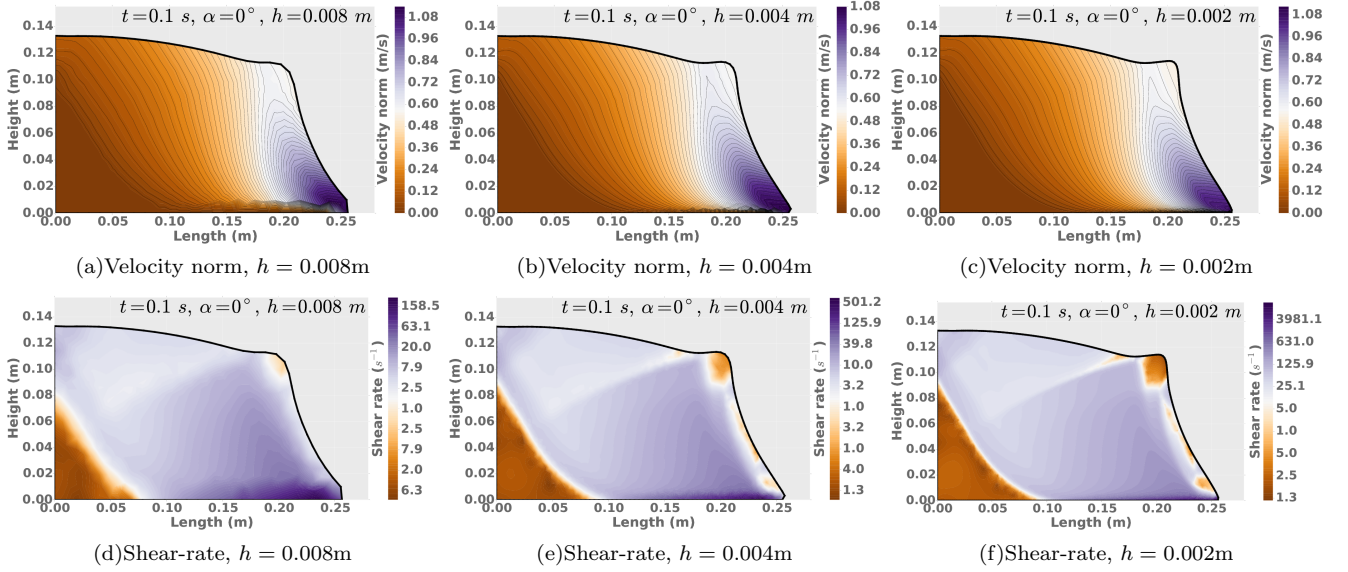


Figure 24. Velocity norm and shear-rate computed at time $t = 0.1\text{s}$ on a slope $\alpha = 0^\circ$ on meshes with cells of size h for a Bingham-like problem with fixed given yield stress $\mu = 100$ in the plasticity criterion. The colorscale of the plots of the shear-rates are logarithmic to enhance readability

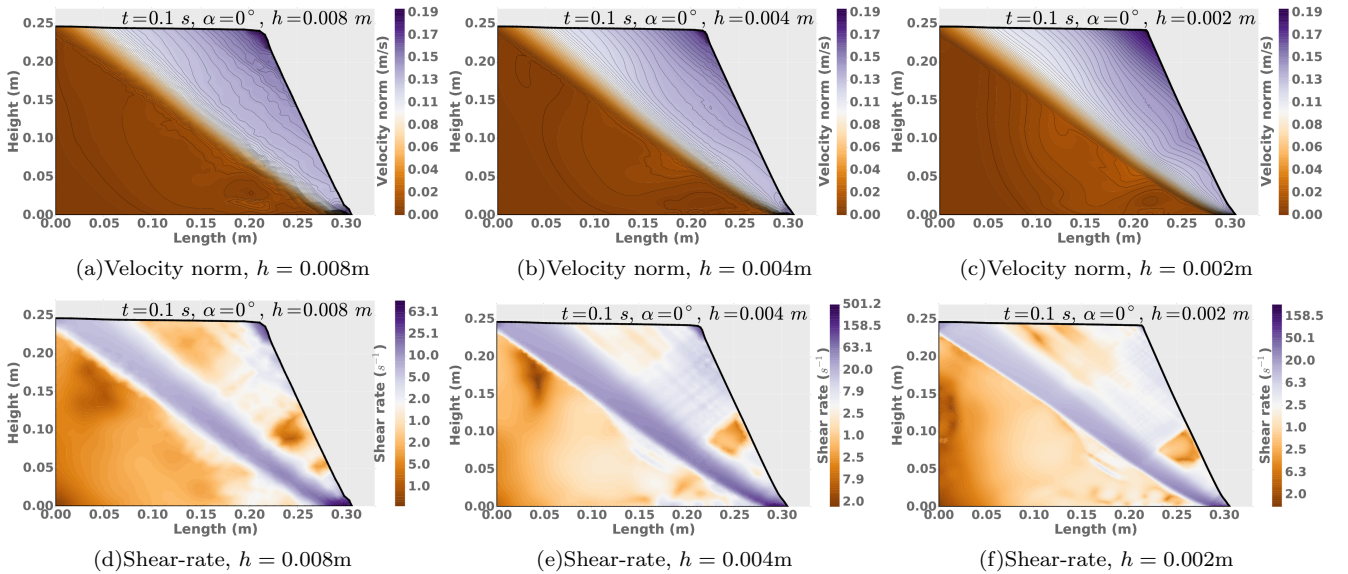


Figure 25. Velocity norm and shear-rate computed at time $t = 0.1\text{s}$ on a slope $\alpha = 0^\circ$ on meshes with cells of size h for a Drucker-Prager problem with a yield stress $\mu = \kappa(p_h)$ where p_h designates the hydrostatic pressure. The colorscale of the plots of the shear-rates are logarithmic to enhance readability.

η_I model fails to do so with the parameters considered here.

+ etude des profils de pression.

ACKNOWLEDGMENTS

Paper text.

Appendix A: Numerical Method

We describe here the numerical algorithm used to solve the dynamic flow problem described above. This numerical method is an extension of the one presented in Ionescu et al.¹⁸ to include lateral friction effects. The following appendix briefly presents the method and its modification and we refer to Ionescu et al.¹⁸ for a more comprehensive description.

The time discretization is achieved using an implicit Euler scheme, and a set of nonlinear equations on the velocity \mathbf{u} , the deviatoric stress tensor \mathbf{S} and the pressure p is to be resolved at each time step.

To overcome the difficulties related to the non-differentiability of the viscoplastic and friction terms, an iterative decomposition-coordination formulation coupled with the augmented Lagrangian method of Glowinski and Le Tallec¹² and Fortin and Glowinski¹⁰ is adapted here.

The treatment of the Coulomb friction condition is done using a regularisation approach (see Ionescu¹⁵, Ionescu¹⁶). A small frictional viscosity $\eta_f \ll 1$ is introduced in the Coulomb friction law (12) which is then written:

$$\mathbf{u}_T = -\frac{1}{\eta_f} \left[1 - \frac{\mu[-\boldsymbol{\sigma}_n]_+}{|\boldsymbol{\sigma}_T|} \right]_+ \boldsymbol{\sigma}_T, \quad (\text{A1})$$

where $[\]_+$ denotes the positive part. The new formulation of the friction law has the same mathematical structure as the viscoplastic constitutive equation (9) and we can use the same iterative decomposition-coordination formulation.

The volume Coulomb friction is treated identically but in that case the tangential stress comes from the 3D formulation (see (18)). If we denote the 3D tangential stress $\boldsymbol{\sigma}_Z$ (in order to avoid confusion), we obtain:

$$\mathbf{u} = -\frac{1}{\eta_w} \left[1 - \frac{\mu[p]_+}{|\boldsymbol{\sigma}_Z|} \right]_+ \boldsymbol{\sigma}_Z. \quad (\text{A2})$$

In the present case, the regularization frictional viscosity coefficient has been set to $\eta_f = \eta_w = 0.1 \text{Pa.s.m}^{-1}$.

The treatment of the free-surface and the associated time-moving domain within a Navier-Stokes problem is achieved through an Arbitrary Lagrangian-Eulerian (ALE) method which is rather classical and thus not described here (see for instance Hughes et al.¹⁴, Maury³⁰, Maronnier et al.²⁸, Duarte et al.⁶).

1. Time discretization

Let Δt be the time step and \mathbf{u}^k , \mathbf{S}^k and p^k be the values of the unknowns at time k . The implicit Euler scheme applied to problem (10) with viscoplastic flow law (9) gives the following set of nonlinear equations on \mathbf{u}^k , \mathbf{S}^k , p^k and $\boldsymbol{\sigma}_Z^k$:

$$\rho \left(\frac{\mathbf{u}^k - \mathbf{u}^{k-1}}{\Delta t} + \mathbf{u}^k \cdot \nabla \mathbf{u}^k \right) - \text{div } \mathbf{S}^k + \nabla p^k + \boldsymbol{\sigma}_Z^k = \rho \mathbf{g} \quad \text{in } \Omega, \quad (\text{A3})$$

$$\text{div}(\mathbf{u}^k) = 0 \quad \text{in } \Omega, \quad (\text{A4})$$

$$\mathbf{D}(\mathbf{u}^k) = \frac{1}{2\eta(\|\mathbf{D}(\mathbf{u}^k)\|, p^k)} \left[1 - \frac{\kappa(p^k)}{\|\mathbf{S}^k\|} \right]_+ \mathbf{S}^k, \quad (\text{A5})$$

$$\mathbf{u}^k = \frac{-1}{\eta_f} \left[1 - \frac{\mu[p]_+}{|\boldsymbol{\sigma}_Z^k|} \right]_+ \boldsymbol{\sigma}_Z^k \quad (\text{A6})$$

while the boundary conditions read

$$\mathbf{S}^k \mathbf{n} = 0 \quad \text{on } \Gamma_s, \quad (\text{A7})$$

$$\mathbf{u}^k \cdot \mathbf{n} = 0, \quad \mathbf{u}_T^k = -\frac{1}{\eta_f} \left[1 - \frac{\mu[-\boldsymbol{\sigma}_n^k]_+}{|\boldsymbol{\sigma}_T^k|} \right]_+ \boldsymbol{\sigma}_T^k, \quad \text{on } \Gamma_b. \quad (\text{A8})$$

2. The algorithm at each time step

Let $r, r_f, r_w > 0$ be the augmented Lagrangian parameters. Let the strain rate multipliers $\dot{\gamma}^{k,n-1} : \Omega \rightarrow \mathbb{R}_S^{3 \times 3}$, the slip rate multipliers $\delta^{k,n-1} : \Gamma_b \rightarrow \mathbb{R}^2$ and the lateral slip rate multiplier $\lambda^{k,n-1} : \Omega \rightarrow \mathbb{R}^2$, be known.

Step 1. The first step consists in solving the following linear Stokes-like problem for the velocity field $\mathbf{u}^{k,n}$ and the pressure $p^{k,n}$:

$$\text{div}(\mathbf{u}^{k,n}) = 0, \quad (\text{A9})$$

$$\rho \left(\frac{\mathbf{u}^{k,n} - \mathbf{u}^{k-1}}{\Delta t} + \mathbf{u}^{k,n-1} \cdot \nabla \mathbf{u}^{k,n} \right) - \text{div} (r \mathbf{D}(\mathbf{u}^{k,n})) + \nabla p^{k,n} - \frac{2}{w} r_w \mathbf{u}^{k,n} = \rho \mathbf{g} + \text{div} (\mathbf{S}^{k,n-1} - r \dot{\gamma}^{k,n-1}) + \frac{2}{w} (\boldsymbol{\sigma}_Z^{k,n-1} - r_w \lambda^{k,n-1}), \quad (\text{A10})$$

with the boundary conditions

$$(r \mathbf{D}(\mathbf{u}^{k,n}) - p^{k,n} \text{Id} + \mathbf{S}^{k,n-1} - r \dot{\gamma}^{k,n-1}) \mathbf{n} = 0, \quad \text{on } \Gamma_s,$$

$$\mathbf{u}^{k,n} \cdot \mathbf{n} = 0, \quad \text{on } \Gamma_b,$$

$$(r \mathbf{D}(\mathbf{u}^{k,n}) - p^{k,n} \text{Id} + \mathbf{S}^{k,n-1} - r \dot{\gamma}^{k,n-1})_T = -r_f \mathbf{u}_T^{k,n} + r_f \delta^{k,n-1} + \boldsymbol{\sigma}_T^{k,n-1}, \quad \text{on } \Gamma_b.$$

Step 2. First we update the viscosity coefficient $\eta = \eta(\|\mathbf{D}(\mathbf{u}^{k,n})\|, p^{k,n})$ and the yield limit $\kappa = \kappa(p^{k,n})$. Then, we compute the strain rate multipliers $\dot{\gamma}^{k,n}$ and the slip rate multipliers $\delta^{k,n}$

$$\dot{\gamma}^{k,n} = \frac{1}{2\eta + r} \left[1 - \frac{\kappa}{\|\mathbf{S}^{k,n-1} + r \mathbf{D}(\mathbf{u}^{k,n})\|} \right]_+ (\mathbf{S}^{k,n-1} + r \mathbf{D}(\mathbf{u}^{k,n})), \quad (\text{A11})$$

$$\delta^{k,n} = -\frac{1}{\eta_f + r_f} \left[1 - \frac{\mu[-\boldsymbol{\sigma}_n^{k,n-1}]_+}{|\boldsymbol{\sigma}_T^{k,n-1} - r_f \mathbf{u}_T^{k,n}|} \right]_+ (\boldsymbol{\sigma}_T^{k,n-1} - r_f \mathbf{u}_T^{k,n}), \quad (\text{A12})$$

$$\lambda^{k,n} = -\frac{1}{\eta_w + r_w} \left[1 - \frac{\mu[p^{k,n-1}]_+}{|\boldsymbol{\sigma}_Z^{k,n-1} - r_w \mathbf{u}^{k,n}|} \right]_+ \quad (\text{B1})$$

$$(\boldsymbol{\sigma}_Z^{k,n-1} - r_w \mathbf{u}^{k,n}), \quad (\text{A13})$$

according to the decomposition-coordination formulation coupled with the augmented Lagrangian method.

Step 3. Finally, we update the stress deviator $\mathbf{S}^{k,n}$, the tangential stress $\boldsymbol{\sigma}_T^{k,n}$ and the lateral stress $\boldsymbol{\sigma}_Z$ using

$$\mathbf{S}^{k,n} = \mathbf{S}^{k,n-1} + r(\mathbf{D}(\mathbf{u}^{k,n}) - \dot{\gamma}^{k,n}),$$

$$\boldsymbol{\sigma}_T^{k,n} = \boldsymbol{\sigma}_T^{k,n-1} - r_f(\mathbf{u}_T^{k,n} - \delta^{k,n}).$$

$$\boldsymbol{\sigma}_Z^{k,n} = \boldsymbol{\sigma}_Z^{k,n-1} - r_w(\mathbf{u}^{k,n} - \lambda^{k,n}).$$

In the present paper, the problem is solved using a finite element formulation. The computational domain Ω is discretized using triangular finite elements. The finite element spaces for the discretization of $\mathbf{u}^{k,n}$ and $p^{k,n}$ are respectively \mathbb{P}_2 continuous and \mathbb{P}_1 continuous. The variables $\mathbf{S}^{k,n}$ and $\dot{\gamma}^{k,n}$ are discretized using \mathbb{P}_1 discontinuous finite elements. The variables $\boldsymbol{\sigma}_T^{k,n}$ and $\delta^{k,n}$ on the one hand, and $\boldsymbol{\sigma}_Z^{k,n}$ and $\lambda^{k,n}$ on the other hand, are discretized using \mathbb{P}_2 continuous finite elements. The solution of the Stokes like problem at step 1 is rather standard and we address the reader to the litterature for the many techniques available (see for instance Pironneau³⁴). The whole implementation of the solver has been achieved using the software *FreeFem++*¹³.

Appendix B: Analytical pressure in the gravity related frame

Let us consider topography related frame (X, Z) and the velocity field $(U(X, Z), W(X, Z))^T$ in this frame. We denote by α the local slope of the topography with respect to the gravity related frame (x, z) and by $(u(x, z), w(x, z))^T$ the velocity field in this frame.

We have for a constant α :

$$\begin{cases} x = X \cos(\alpha) - Z \sin(\alpha) \\ z = X \sin(\alpha) + Z \cos(\alpha) \end{cases}$$

or equivalently:

$$\begin{cases} X = x \cos(\alpha) + z \sin(\alpha) \\ Z = -x \sin(\alpha) + z \cos(\alpha) \end{cases}$$

The analytical pressure in (X, Z) is given by:

$$p(X, Z) = \rho g (\cos(\alpha) + \sin(\alpha) \partial_X h(X) - 2|\sin(\alpha)| \frac{\partial_X U(X, Z)}{|\partial_Z U(X, Z)|} (h(X) - Z),$$

where $h(X) = Z_s$, Z_s designating the height of the free-surface in (X, Z) (*i.e.* the local thickness of the flow at X). If we denote by $h(x) = z_s$ the height of the free-surface at x , it follows that:

$$\begin{aligned} h(X) &= -x \sin(\alpha) + z_s \cos(\alpha) \\ &= -x \sin(\alpha) + h(x) \cos(\alpha) \end{aligned} \quad (\text{B2})$$

Thus:

$$\begin{aligned} \partial_X h(X) &= -\sin(\alpha) \partial_X x + \cos(\alpha) \partial_X h(x) \\ &= -\sin(\alpha) \cos(\alpha) + \cos(\alpha) \partial_X h(x) \end{aligned} \quad (\text{B3})$$

that becomes, using the chain rule:

$$\partial_X h(X) = \cos^2(\alpha) \partial_x h(x) - \sin(\alpha) \cos(\alpha). \quad (\text{B4})$$

And we also have:

$$h(X) - Z = (h(x) - z) \cos(\alpha) \quad (\text{B5})$$

The change of variable naturally gives:

$$U(X, Z) = u(x, z) \cos(\alpha) + w(x, z) \sin(\alpha) \quad (\text{B6})$$

A similar calculation gives, using the chain rule:

$$\begin{aligned} \partial_X U &= (\partial_x u \cos(\alpha) + \partial_z u \sin(\alpha)) \cos(\alpha) \\ &\quad + (\partial_x w \cos(\alpha) + \partial_z w \sin(\alpha)) \sin(\alpha), \end{aligned} \quad (\text{B7})$$

$$\begin{aligned} \partial_Z U &= (-\partial_x u \sin(\alpha) + \partial_z u \cos(\alpha)) \cos(\alpha) \\ &\quad + (-\partial_x w \sin(\alpha) + \partial_z w \cos(\alpha)) \sin(\alpha). \end{aligned} \quad (\text{B8})$$

We finally obtain using (B4), (B5), (B7) and (B8) in (B1):

$$\begin{aligned} p(x, z) &= \rho g \left(\cos(\alpha) + \sin(\alpha) (\cos^2(\alpha) \partial_x h(x) - \sin(\alpha) \cos(\alpha)) \right. \\ &\quad \left. - 2|\sin(\alpha)| \left[\left((\partial_x u \cos(\alpha) + \partial_z u \sin(\alpha)) \cos(\alpha) + \right. \right. \right. \\ &\quad \left. \left. (\partial_x w \cos(\alpha) + \partial_z w \sin(\alpha)) \sin(\alpha) \right) / \right. \\ &\quad \left. \left. \left| \left((-\partial_x u \sin(\alpha) + \partial_z u \cos(\alpha)) \cos(\alpha) + \right. \right. \right. \right. \\ &\quad \left. \left. \left. (-\partial_x w \sin(\alpha) + \partial_z w \cos(\alpha)) \sin(\alpha) \right) \right| \right] \right) (h - z \cos(\alpha)). \end{aligned} \quad (\text{B9})$$

REFERENCES

- ¹C. Ancey, P. Coussot, P. Evesque, A theoretical framework for very concentrated granular suspensions in steady simple shear flow, *J. Rheol.* 43 (1999) 1673–1699.
- ²B. Andreotti, Y. Forterre, and O. Pouliquen, *Les milieux granulaires, entre fluide et solide*, Savoirs Actuels, EDP sciences, 2011.
- ³E.C. Bingham, *Fluidity and plasticity*, Mc Graw-Hill, New-York, 1992.
- ⁴Bouchut, F., Ionescu, I., and Mangeney, A., 2015. A shallow model including static-flowing transition for viscoplastic Drucker-Prager materials, *Comm. Math. Sci.*, submitted.

- ⁵G. B. Crosta, S. Imposimato, D. Roddeman Wright, R. Y. Yang, B. H. Xu, and A. B. Yu, Numerical modeling of 2-D granular step collapse on erodible and non-erodible surface, *J. Geophys. Res.* 114 (2009), F03020, doi:10.1029/2008JF001186.
- ⁶F. Duarte, R. Gormaz and S. Natesan, Arbitrary Lagrangian Eulerian method for Navier Stokes equations with moving boundaries, *Comput. Methods Appl. Mech. Engrg.* 193 (2004), 4819-4836.
- ⁷G. Duvaut, and J.-L. Lions, *Les inéquations en mécanique et en physique*, Dunod, Paris, 1972.
- ⁸E.E. Doyle, H.E. Huppert, G. Lube, H.M. Mader, and R.S.J. Sparks, Static and flowing regions in granular collapses down channels: Insights from a sedimenting shallow water model, *Phys. Fluids* 19 (2007), 106601.
- ⁹M. Farin and A. Mangeney and O. Roche, Fundamental changes of granular flow dynamics, deposition, and erosion processes at high slope angles: Insights from laboratory experiments, *JGR: Earth Surface*. 119 (2014) 504-532.
- ¹⁰M. Fortin, and R. Glowinski, *Méthodes de Lagrangien augmenté, application à la résolution de problèmes aux limites*, Dunod, 1982.
- ¹¹L. Girolami, V. Hergault, G. Vinay, and A. Wachs, A three-dimensional discrete-grain model for the simulation of dam-break rectangular collapses: Comparison between numerical results and experiments, *Granular Matter* 14 (2012), 381-392.
- ¹²R. Glowinski, and P. Le Tallec, *Augmented Lagrangian and Operator Splitting method in Non-Linear Mechanics*, SIAM Studies in Applied Mathematics, 1989.
- ¹³Hecht, F. New development in FreeFem++. *J. Numer. Math.* 20 (2012), no. 3-4, 251–265. 65Y15.
- ¹⁴T. Hughes, W. Liu, and T. Zimmermann, Lagrangian-Eulerian finite element formulation for incompressible viscous flows, *Comput. Methods Appl. Mech. Engrg.* 29 (1981), 329-349.
- ¹⁵I.R. Ionescu, Onset and dynamic shallow flow of a viscoplastic fluid on a plane slope, *J. Non-Newtonian Fluid Mechanics* Vol. 165,19-20 (2010), 1328-1341.
- ¹⁶I.R. Ionescu, Augmented Lagrangian for shallow viscoplastic flow with topography, *Journal of Computational Physics* 242 (2013), 544-560.
- ¹⁷I.R. Ionescu, Viscoplastic shallow flow equations with topography, *J. Non-Newtonian Fluid Mechanics* 193 (2013), 116-128.
- ¹⁸I.R. Ionescu, A. Mangeney, F. Bouchut, O. Roche, Viscoplastic modeling of granular column collapse with pressure-dependent rheology. *J. of Non-Newtonian Fluid Mech.* 219 (2015) 1-18.
- ¹⁹P. Jop, Y. Forterre, O. Pouliquen, A constitutive law for dense granular flows, *Nature* 441 (2006) 727–730.
- ²⁰P. Jop, Y. Forterre, and O. Pouliquen, Crucial role of sidewalls in dense granular flows: consequences for the rheology, *J. Fluid Mech.* 541 (2005), 167-192.
- ²¹R.R. Kerswell, Dam break with coulomb friction: a model for granular slumping, *Phys. Fluids* 17 (2005), 057101.
- ²²L. Lacaze, and R.R. Kerswell, Axisymmetric granular collapse: a transient 3D flow test of viscoplasticity, *Phys. Rev. Lett.* 102 (2009), 108305.
- ²³L. Lacaze, J. Phillips, and R.R. Kerswell, Planar collapse of a granular column: experiments and discrete-element simulations, *Phys. Fluids* 20 (2008), 063302.
- ²⁴P.-Y. Lagrée, L. Staron, and S. Popinet, The granular column collapse as a continuum: validity of a two-dimensional Navier-Stokes model with a $\mu(I)$ -rheology, *J. Fluid Mech.* 686 (2011), 378-408.
- ²⁵E. Larrieu, L. Staron, and E. J. Hinch, Raining into shallow water as a description of the collapse of a column of grains, *J. Fluid Mech.* 554 (2006), 259.
- ²⁶A. Mangeney-Castelnau, F. Bouchut, J.-P. Vilotte, E. Lajeunesse, A. Aubertin, and M. Pirulli, On the use of Saint-Venant equations to simulate the spreading of a granular mass, *J. Geophys. Res.* 110 (2005), B09103, doi:10.1029/2004JB003161.
- ²⁷A. Mangeney and O. Roche and O. Hungr and N. Mangold and G. Faccanoni and A. Lucas, Erosion and mobility in granular collapse over sloping beds. *JGR: Earth Surface*. 115,F03040 (2010).
- ²⁸V. Maronnier, M. Picasso, and J. Rappaz, Numerical simulation of three dimensional free surface flows, *Int. J. Numer. Method in Fluids* 42 (2003), 697-716.
- ²⁹N. Martin, J. Monnier, Inverse rheometry and basal properties inference for pseudoplastic geophysical flows, *European Journal of Mechanics - B/Fluids*. 50 (2014) 110-126.
- ³⁰B. Maury, Characteristics ALE method for the unsteady 3D Navier-Stokes equations with a free surface, *Int. J. Comp. Fluid Dyn.* 6 (1996), 175-188.
- ³¹C. Meruane, A. Tamburrino, and O. Roche, On the role of the ambient fluid on gravitational granular flow dynamics, *J. Fluid Mech.* 648 (2010), 381.
- ³²GDR MiDi group, On dense granular flows, *Eur. Phys. J. E14* (2004), 341-365.
- ³³P. Perzyna, Fundamental problems in viscoplasticity, *Adv. Appl. Mech.* 9, 243-377.
- ³⁴O. Pironneau, *Finite element methods for fluids*, John Wiley & Sons Ltd., Chichester, 1989.
- ³⁵S.B. Savage, The mechanics of rapid granular flows, *Adv. Appl. Mech.* 24 (1984) 289–366.
- ³⁶L.E. Silbert et al., Granular flow down an inclined plane: Bagnold scaling and rheology, *Phys. Rev. E* 64 (2001), 051302.
- ³⁷L. Staron, and E.J. Hinch, Study of the collapse of granular columns using 2D discrete-grains simulation, *J. Fluid Mech.* 545 (2005), 1.
- ³⁸N. Taberlet, P. Richard, A. Valance, R. Delannay, W. Losert, J.M. Pasini, and J.T. Jenkins, Super stable granular heap in thin channel, *Phys. Rev. Lett.* 91 (2003), 264301.
- ³⁹R. Zenit, Computer simulations of the collapse of a granular column, *Phys. Fluids* 17 (2005), 031703.